ARMY RESEARCH LABORATORY

Unsteady Aerodynamic Simulations of a Finned Projectile at a Supersonic Speed With Jet Interaction

by Jubaraj Sahu, Frank Fresconi, and Karen R. Heavey

ARL-TR-6960 **June 2014**

NOTICES

Disclaimers

The findings in this report are not to be construed as an official Department of the Army position unless so designated by other authorized documents.

Citation of manufacturer's or trade names does not constitute an official endorsement or approval of the use thereof.

Destroy this report when it is no longer needed. Do not return it to the originator.

Army Research Laboratory
Aberdeen Proving Ground, MD 21005-5069

ARL-TR-6960 **June 2014**

Unsteady Aerodynamic Simulations of a Finned Projectile at a Supersonic Speed With Jet Interaction

Jubaraj Sahu, Frank Fresconi, and Karen R. Heavey
Weapons and Materials Research Directorate, ARL

REPORT DOCUMENTATION PAGE	Form Approved OMB No. 0704-0188

1. REPORT DATE *(DD-MM-YYYY)*	2. REPORT TYPE	3. DATES COVERED (From - To)
June 2014	Final	January 2012–May 2013

4. TITLE AND SUBTITLE

Unsteady Aerodynamic Simulations of a Finned Projectile at a Supersonic Speed With Jet Interaction

5a. CONTRACT NUMBER

5b. GRANT NUMBER

5c. PROGRAM ELEMENT NUMBER

6. AUTHOR(S)

Jubaraj Sahu, Frank Fresconi, and Karen R. Heavey

5d. PROJECT NUMBER

5e. TASK NUMBER

5f. WORK UNIT NUMBER

7. PERFORMING ORGANIZATION NAME(S) AND ADDRESS(ES)

U.S. Army Research Laboratory
ATTN: RDRL-WML-E
Aberdeen Proving Ground, MD 21005-5069

8. PERFORMING ORGANIZATION REPORT NUMBER

ARL-TR-6960

9. SPONSORING/MONITORING AGENCY NAME(S) AND ADDRESS(ES)

10. SPONSOR/MONITOR'S ACRONYM(S)

11. SPONSOR/MONITOR'S REPORT NUMBER(S)

12. DISTRIBUTION/AVAILABILITY STATEMENT

Approved for public release; distribution is unlimited.

13. SUPPLEMENTARY NOTES

14. ABSTRACT

This report describes a computational study to understand the unsteady free-flight aerodynamics and flight dynamics of a finned projectile with jet control. Numerical simulations have been performed for this projectile with jet maneuver using an advanced coupled computational fluid dynamics (CFD)/rigid body dynamics (RBD) technique. The coupled CFD/RBD method allows time-accurate virtual fly-out simulations of projectiles and simultaneously predicts the aerodynamics and the flight dynamics in an integrated manner. The control is provided by a transient pulsed jet that is activated only once in the beginning for a fixed duration and then turned off for the remaining trajectory computation. Computed results show the actual time-dependent response of the flight vehicle and the resulting unsteady aerodynamics and flight dynamics with jet control for a variety of conditions.

15. SUBJECT TERMS

coupled fly-outs, jet interaction, pulsed jet, jet control, computational fluid dynamics

16. SECURITY CLASSIFICATION OF:			17. LIMITATION OF ABSTRACT	18. NUMBER OF PAGES	19a. NAME OF RESPONSIBLE PERSON
a. REPORT	b. ABSTRACT	c. THIS PAGE			Jubaraj Sahu
Unclassified	Unclassified	Unclassified	UU	52	19b. TELEPHONE NUMBER (*Include area code*) 410-306-0798

Standard Form 298 (Rev. 8/98)
Prescribed by ANSI Std. Z39.18

Contents

List of Figures

List of Tables

Acknowledgments

This work was accomplished as part of a grand challenge project jointly sponsored by the Department of Defense High Performance Computing Modernization program and the U.S. Army Research Laboratory. The authors wish to thank Dr. Sukumar Chakravarthy of Metacomp Technologies for providing expert advice and help with the coupled computational fluid dynamics/rigid body dynamics virtual fly-out simulations and in particular with the time-dependent jet boundary condition. The authors also wish to thank Dr. Jim DeSpirito and Dr. Paul Weinacht for providing many helpful suggestions and a thorough review of this report.

1. Introduction

As part of a Department of Defense High Performance Computing (HPC) grand challenge project, the U.S. Army Research Laboratory has recently focused on the development and application of state-of-the art numerical approaches for large-scale simulations (*1–4*) to determine both steady and unsteady aerodynamics and flight dynamics of projectiles with and without flow control. Accurate determination of aerodynamics and flight dynamics is critical to the low-cost development of new affordable munitions. Our objective is to exploit computational fluid dynamics (CFD) techniques on HPC platforms for design and analysis of guided projectiles. For these maneuvering munitions, the effect of many weapon control mechanisms, such as canards, deployable pins, flaps, and jets/microjets (steady or pulsed) on flight dynamics is critical to guided flight performance (*5–13*). The control forces are provided through the action of these control mechanisms.

The goal is to determine if these control devices can provide the desired control authority for course correction for munitions. Many of these mechanisms fall outside the range of conventional aerodynamic control, and accurate well-validated tools for prediction of aerodynamic loads are desired. These control mechanisms result in highly complex, unsteady flow interactions, and their accurate modeling during guided flight with active control is a major challenge. Knowledge of the detailed aerodynamics of maneuvering guided smart weapons is rather limited. Time-accurate CFD and multidisciplinary coupled CFD and rigid body dynamics (RBD) techniques are needed to provide detailed fluid dynamic understanding of the unsteady aerodynamics processes involving the maneuvering flight of modern guided weapon systems. Such knowledge cannot be obtained easily by any other means. The multidisciplinary technique has great potential and can lead to better experimental designs and much better returns for full-scale flight experiments. More importantly, they can provide physical insight of fluid mechanic processes that may not be gained from experimental techniques and flight tests.

Significant progress has been made recently with the computational technology involving CFD and RBD for prediction of unsteady aerodynamics and flight dynamics of projectiles without control maneuvers (*14–18*). The computational technology involving CFD and RBD can be considered mature as independent disciplines, and should be exploited to determine the unsteady aerodynamics associated with control maneuvers. The CFD part is still the major contributor in the coupled CFD/RBD simulations and accounts for most of the time used. The advanced CFD capability used here to solve the unsteady Navier-Stokes equations (*19*) incorporates unsteady boundary conditions and a special coupling procedure. Research over the past few years has been carried out on "virtual fly-outs" of projectiles on the supercomputers, which allow numerical prediction of the actual flight paths of a projectile and all the associated unsteady free-flight aerodynamics using coupled CFD/RBD techniques in an integrated manner (*3, 16*). Validation of

the computed results from the virtual fly-out simulations was accomplished by comparison with free-flight test data. Very recently, a flight control system (FCS) has been integrated with the CFD/RBD procedure to extend the capability of the coupled technique further for simulation of guided control maneuvers. The resulting coupled CFD/RBD/FCS capability has initially been demonstrated on a canard-controlled projectile using a roll control and a cross-range control (*20*). Further development is needed to extend the capability of this technique for determining the unsteady aerodynamics and flight dynamics associated with conventional and new aerodynamic control technologies for maneuvering munitions.

Before a fully coupled CFD/RBD/FCS capability is established for guided trajectory control with a jet as the control mechanism, we need to develop a fully coupled CFD/RBD capability for the same without the FCS component. The present work is therefore focused on the continued development and application of the coupled CFD and RBD techniques for simultaneous prediction of the unsteady free-flight aerodynamics and the flight dynamics of projectiles with a normal jet control maneuver. Activating a jet generates control forces and, thus, provides the control authority needed to maneuver the flight vehicle. The resulting flow field is highly three-dimensional (3-D), unsteady, and very complex, with shock structures and separated flow regions even at small angles of attack. This is especially true at high angles of attack where the flow field is complex even without jet interaction. Slender bodies at high angle of attack exhibit complicated flow structures such as asymmetric vortex shedding that induce nonlinear side forces and side moments (*21*). One must take into account the jet interaction effects to be able to predict the overall aerodynamic forces and moments acting on the projectile at low to high angles of attack. Accurate numerical modeling of the unsteady aerodynamics can be challenging and generally requires the use of time-accurate CFD or coupled CFD/RBD solution techniques.

Examples of experimental and numerical studies of lateral jet interaction on a finned projectile include both steady-state jets and transient pulse jets (*22–26*). Time-accurate CFD was used recently in the case of a pulse jet (*27*). The present work offers an alternate approach and takes into account precisely the jet interaction effect as would be seen in actual flight. It is an extension of earlier research on coupled CFD/RBD virtual fly-out technique (*3, 17*) to the free-flight aerodynamics and flight dynamics of a jet controlled projectile where jets are used to provide the control authority needed to maneuver the projectile. This technique also includes any coupling effect due to the projectile motion. The objective is to show the capability of the coupled virtual fly-out technique (*3*) to predict the unsteady aerodynamics and flight dynamics of a finned projectile with a pulse jet control. The following sections describe the coupled numerical procedure and the computed results obtained with jet maneuver flight of the finned projectile at a supersonic speed.

2. Solution Technique

2.1 Flow Solver

Research efforts are ongoing to perform time-accurate multidisciplinary coupled CFD/RBD computations for complex guided projectiles. In the present work, a time-accurate numerical approach is used. This approach requires that the six-degrees-of-freedom (6DOF) body dynamics be computed at each repetition of a flow solver. The CFD capability used here solves the Navier-Stokes equations and incorporates advanced boundary conditions and grid motion capabilities.

The complete set of 3-D time-dependent Navier-Stokes equations is solved in a time-accurate manner for simulations of virtual fly-outs. A commercially available code, CFD++ (*28, 29*), is used for the time-accurate unsteady CFD simulations. The 3-D time-dependent Reynolds-averaged Navier-Stokes equations are solved using the following finite volume method:

$$\frac{\partial}{\partial t}\int_V \mathbf{W} dV + \oint [\mathbf{F} - \mathbf{G}] \cdot dA = \int_V \mathbf{H} dV \tag{1}$$

where **W** is the vector of conservative variables, **F** and **G** are the inviscid and viscous flux vectors, respectively, **H** is the vector of source terms, V is the cell volume, and A is the surface area of the cell face.

Several techniques, such as implicit local time-stepping and relaxation are used to achieve faster convergence. Use of an implicit scheme circumvents the stringent stability limits suffered by their explicit counterparts, and successive relaxation allows update of cells as information becomes available and thus aids convergence. Second-order discretization was used for the flow variables and the turbulent viscosity equation. The turbulence closure is based on topology-parameter-free formulations. Two-equation turbulence models (*30, 31*) were used for the computation of turbulent flows. These models are ideally suited to unstructured bookkeeping and massively parallel processing due to their independence from constraints related to the placement of boundaries and/or zonal interfaces.

For time-accurate simulations of virtual fly-outs that are of interest here, dual time-stepping as described in the following was used to achieve the desired time accuracy. The whole grid was actually moved to take into account the spinning motion of the projectile.

2.2 Dual Time-Stepping

The “dual time-stepping mode” of the code was used to perform the transient flow simulations. The term “dual time-step” implies the use of two time steps. The first one is an “outer” or global (and physical) time step that corresponds to the time discretization of the physical time variation

term. This time step can be chosen directly by the user and is typically set to a value to represent 1/100 of the period of oscillation expected or forced in the transient flow. This time step is applied to every cell (not separately varying).

An artificial "inner" or "local" time variation term is added to the basic physical equations. This time step and corresponding "inner-iteration" strategy is chosen to help satisfy the physical transient equations to the desired degree. If the inner iterations converge, the outer physical transient equations (their discretization) are satisfied exactly; otherwise, they are approximately satisfied. The time step for the inner iterations is allowed to vary spatially. Also, relaxation with algebraic multigrid acceleration is employed to reduce the residuals of the physical transient equations. An order of magnitude reduction in the residuals is usually sufficient to produce a good transient iteration. This may require a few internal iterations to achieve, i.e., between 10 and 20 depending on the magnitude of the outer time step, the nature of the problem, the nature of the boundary conditions, and the consistency of the mesh with respect to the physics at hand.

2.3 Grid Movement

Grid velocity is assigned to each mesh point. This general capability can be tailored for many specific situations. For example, the grid point velocities can be specified to correspond to a spinning projectile. In this case, the grid speeds are assigned as if the grid is attached to the projectile and spinning with it. Similarly, to account for rigid body dynamics, the grid point velocities can be set as if the grid is attached to the rigid body with 6DOF.

2.4 Six-Degrees-of-Freedom Modeling

Rigid-body projectile flight states are position (x, y, z), attitude (ϕ, θ, ψ), body translational velocity (u, v, w), and body rotational velocity (p, q, r). The kinematic equations of flight are derived in the body-fixed coordinate system (*32*). Quaternions are used to integrate the rotational kinematics; however, the appropriate relationships are implemented to express attitude in Euler angles (ϕ, θ, ψ) when desired. The shorthand notation is used for trigonometric functions [e.g., $\sin(\phi) = s_\phi$].

$$\begin{bmatrix}\dot{x}\\ \dot{y}\\ \dot{z}\end{bmatrix} = \begin{bmatrix}c_\theta c_\psi & s_\phi s_\theta c_\psi - c_\phi s_\psi & c_\phi s_\theta c_\psi + s_\phi s_\psi\\ c_\theta s_\psi & s_\phi s_\theta s_\psi + c_\phi c_\psi & c_\phi s_\theta c_\psi + s_\phi s_\psi\\ -s_\theta & s_\phi c_\theta & c_\phi c_\theta\end{bmatrix}\begin{bmatrix}u\\ v\\ w\end{bmatrix} \tag{2}$$

$$\begin{bmatrix}\dot{q}_0\\ \dot{q}_1\\ \dot{q}_2\\ \dot{q}_3\end{bmatrix} = \begin{bmatrix}0 & -p & -q & -r\\ p & 0 & r & -q\\ q & -r & 0 & p\\ r & q & -p & 0\end{bmatrix}\begin{bmatrix}q_0\\ q_1\\ q_2\\ q_3\end{bmatrix} \tag{3}$$

Equations for the body-fixed flight dynamics follow.

$$\begin{bmatrix}\dot{u}\\ \dot{v}\\ \dot{w}\end{bmatrix} = \frac{1}{m}\begin{bmatrix}X + X_G\\ Y + Y_G\\ Z + Z_G\end{bmatrix} - \begin{bmatrix}0 & -r & q\\ r & 0 & -p\\ -q & p & 0\end{bmatrix}\begin{bmatrix}u\\ v\\ w\end{bmatrix} \tag{4}$$

$$\begin{bmatrix}\dot{p}\\ \dot{q}\\ \dot{r}\end{bmatrix} = \vec{I}^{-1}\begin{bmatrix}L\\ M\\ N\end{bmatrix} - \vec{I}^{-1}\begin{bmatrix}0 & -r & q\\ r & 0 & -p\\ -q & p & 0\end{bmatrix}\vec{I}\begin{bmatrix}p\\ q\\ r\end{bmatrix} \tag{5}$$

The following relationship was used to determine the gravity forces acting on the projectile.

$$\begin{bmatrix}X_G\\ Y_G\\ Z_G\end{bmatrix} = \begin{bmatrix}-s_\theta mg\\ s_\phi c_\theta mg\\ c_\phi c_\theta mg\end{bmatrix} \tag{6}$$

2.5 Aerodynamics and Jet Assessment

Two methods were applied in this study to calculate the aerodynamic and jet forces (X, Y, Z) and moments (L, M, N) used in the right-hand side of equations 4 and 5, which dictate the projectile flight motion. One method, referred to hereafter as the aerodynamic model/RBD method, is the conventional approach used throughout the aerospace community. In this method, aerodynamic coefficients are quantified off-line through techniques such as semi-empirical aeroprediction, wind tunnel tests, CFD, or range tests. An appropriate mathematical model that uses look-up tables of these aerodynamic coefficients is implemented in flight simulation to compute aerodynamic forces and moments at each time step.

The other method, called coupled CFD/RBD, utilizes CFD at each flight simulation time step to calculate the aerodynamic forces and moments required for the flight dynamic equations. The flight response resulting from integrating equations 2–5 are subsequently used to move the grid (locations and velocities) for CFD in the next time step. While the coupled CFD/RBD method is more computationally expensive than the aerodynamic model/RBD method, this approach permits more detailed insight into the fundamental flight behaviors. Regardless of the aerodynamics assessment method, the RBD equations are the same.

In addition to the coupled mode, CFD++ features an uncoupled mode, which is useful for debugging and initialization. In the uncoupled mode, the aerodynamic forces and moments from CFD are not coupled with the rigid body dynamics module.

2.6 Aerodynamic and Jet Modeling for 6DOF Simulation Without CFD Coupling

More traditional flight simulations were conducted to compare with the coupled CFD/RBD results. In this scenario, aerodynamic data must be inserted to a mathematical model to drive the right-hand side of the flight dynamics (equations 4–5).

The body-fixed coordinate system is shown in figure 1 to provide a sense for positive body parameters (e.g., forces and moments) and motivate the definition of angle of attack. Body translational velocities are used to determine the angle of attack (α) and angle of sideslip (β).

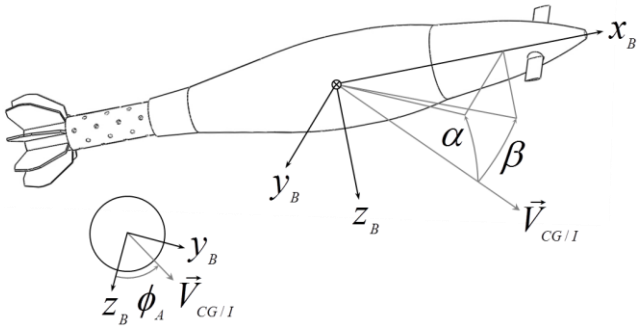

Figure 1. Aerodynamic angles of attack and body-fixed coordinate system.

$$\alpha = asin\left[\frac{w}{\sqrt{u^2 + w^2}}\right] \tag{7}$$

$$\beta = asin\left[\frac{v}{\sqrt{u^2 + v^2 + w^2}}\right] \tag{8}$$

Angles of attack are sometimes expressed in the fixed-plane coordinate system in this report. To obtain these quantities, the body-fixed translational velocities are first transformed to fixed-plane coordinates (symbols with tilde on top) prior to using equations 7 and 8 to calculate fixed-plane angle of attack. Total angle of attack is simply the root-sum-square of angle of attack and angle of sideslip.

$$\begin{bmatrix}\tilde{u}\\ \tilde{v}\\ \tilde{w}\end{bmatrix} = \begin{bmatrix}1 & 0 & 0\\ 0 & c_\phi & -s_\phi\\ 0 & s_\phi & c_\phi\end{bmatrix}\begin{bmatrix}u\\ v\\ w\end{bmatrix} \tag{9}$$

The aerodynamic model used in the traditional flight dynamics analysis is shown in equations 10–15. The model includes nonlinearity with Mach and angle of attack and static and dynamic terms. The dynamic terms are dynamic side force (C_{Y_p}), roll damping moment (C_{l_p}), pitch damping moment (C_{m_q}), and dynamic side moment (C_{n_p}).

$$X = -QSC_X(M, \bar{\alpha}) \tag{10}$$

$$Y = -QS\left[C_N(M, \beta) - C_{Y_p}(M, \alpha)\frac{pD}{2V}\right] \tag{11}$$

$$Z = -QS\left[C_N(M,\alpha) - C_{Y_p}(M,\beta)\frac{pD}{2V}\right] \tag{12}$$

$$L = QSDC_{l_p}(M,\bar{\alpha})\frac{pD}{2V} \tag{13}$$

$$M = QSD\left[C_m(M,\alpha) + C_{m_q}(M)\frac{qD}{2V} + C_{n_p}(M,\beta)\frac{pD}{2V}\right] \tag{14}$$

$$N = QSD\left[-C_m(M,\beta) + C_{m_q}(M)\frac{rD}{2V} + C_{n_p}(M,\alpha)\frac{pD}{2V}\right] \tag{15}$$

Basic aerodynamic data without jet interaction came from a previous computational study (*33*). These computational CFD data, which consisted of both static and dynamic aerodynamic coefficients, were obtained using steady-state and transient calculations for the same projectile and covered a range of angle of attack from –10° to 90°. The projectile underwent prescribed motions to obtain dynamic derivatives. Symmetry was invoked to obtain all components of force and moment coefficients as needed. These data were used in look-up tables of Mach and angle of attack in an aerodynamic model. The jet forces and moments were modeled as a simple force and moment. The jet interaction effects came from steady-state jet calculations performed as part of this study. The aerodynamic forces and moments calculated from this aerodynamic model and data were used in the body-fixed 6DOF model outlined previously to determine the projectile flight. This essentially constitutes the standard aerodynamic model/RBD simulation procedure.

2.7 Solution Initialization for Coupled CFD/RBD Method

Typical coupled method simulations begin with a computation performed in "steady-state mode" with the grid velocities prescribed to account only for the translational motion component of the complete set of initial conditions to be prescribed. At this stage we also impose the angular orientations from the initial conditions. The complete set of initial conditions includes both translational and rotational velocity components along with initial position and angular orientation. We obtain the steady-state solution with a fixed translational velocity. This solution becomes the initial condition for the next step which involves adding just the spin component of the projectile. With the addition of spin, time-accurate calculations are performed for a few cycles of spin until converged periodic forces and moments are obtained. A sufficient number of time steps are performed so that the angular orientation for the spin axis corresponds to the prescribed initial conditions. This computation is performed in an uncoupled mode. The mesh is translated back to the desired initial position, the pitch and yaw rates are turned on, and computations are carried out in the coupled mode. For cases with jet control maneuvers, pulse

jets are not used during the steady state as well as the time-accurate uncoupled solution stages. The jet is activated during the time-accurate virtual fly-out simulation in the coupled mode only using a new time-dependent jet boundary condition described as follows.

2.8 Time-Dependent Jet Boundary Condition

A new jet inflow boundary condition (BC) was added to CFD++ code by Metacomp Technologies, Inc., to run simulations where the jet is turned on and off in several different ways.

- The BC starts out as a time-dependent total-pressure, total-temperature imposition type of inflow BC. The time dependency is specified in a suitable input file where each variable (total pressure, total temperature, any turbulence variables, etc.) is defined as a function of time. This can be used to ramp up or ramp down the total pressure under full user control.
- When the total pressure imposed becomes less than the local static pressure in the course of a run, the BC automatically converts to be a wall BC where the inlet velocity is zero.
- The BC is sensitized to rotation automatically. This means that the inflow velocities are rotating (in the tangent plane to the inflow surface) along with the body. This feature is active when there is any grid rotation effects turned on (e.g., through RBD coupling).
- The time dependency can be replaced as a dependency on the current chosen Euler angle value or the current rotational angle value. These options require RBD mode in the code to be active. The rotational angles are obtained by an integration of the rotational rates about each axis in the body frame.
- There is an additional control being built to turn this jet on and off where the on and off controls are based on coupled co-simulation with a FCS module. When the jet is in the off state through this on-off control, the BC reverts to that of a wall. This type of control would be needed for coupled simulations of guided jet control.

3. Model Geometry and Grid

The projectile modeled in this study is the basic finner, a cone-cylinder-finned configuration (*33, 34*). A schematic diagram of the basic finner shape is shown in figure 2. The length of the projectile is 10 cal. and the diameter is 30 mm. The conical nose is 2.84 cal. long and is followed by a 7.16-cal cylindrical section. Four rectangular planform fins are located on the back end of the projectile. Each fin is 1 cal. long, has a sharp leading edge, and has a thickness of 0.08 cal. at the trailing edge. These fins have no cant. The center of gravity is located 5.5 cal. from the nose of the projectile.

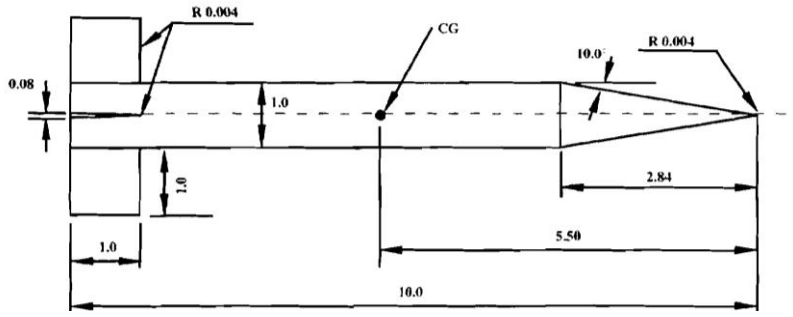

Figure 2. Schematics of the basic finned configuration
(dimensions in calibers; 1 cal. = 0.03 m).

Figures 3a and 3b show the 3-D computational models of the finned projectile and the nozzle geometry for the jet, respectively. There are four nozzles spaced equally in the circumferential direction as shown in figure 3b. Axially, these nozzles are located just downstream of the nose-cylinder junction, 90 mm from the nose of the projectile. Each nozzle is 9.5 mm long with a jet inlet diameter of 10 mm and a jet exit diameter of 2.6 mm. In the present study, only one nozzle is used and the time-dependent jet boundary condition described is applied at the bottom surface of the nozzle. All four nozzles could be used in future numerical studies so each nozzle jet can be turned on and off as needed for guided jet control flights. The pulse jets are intended to generate control forces/moments and the control authority needed to maneuver the projectile.

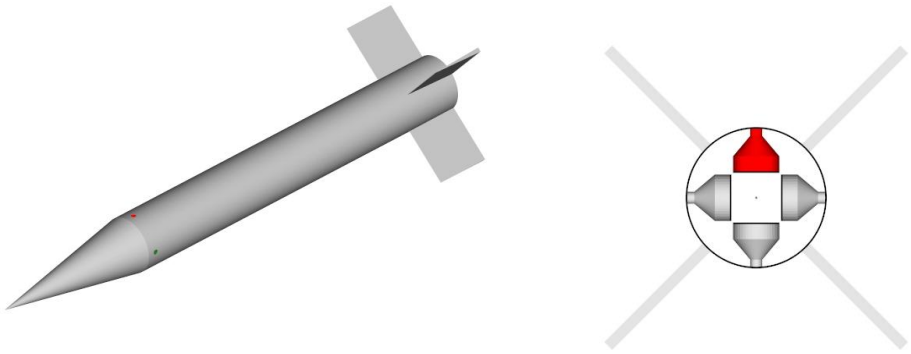

(a) **(b)**

Figure 3. Finned projectile geometry: (a) full model and (b) nozzle jet geometry.

A structured hexahedral mesh was created for this projectile geometry using GRIDGEN, a commercially available grid generation software (*35*). A blocked-zonal methodology was used to facilitate meshing by allowing replacement grid blocks in the area of interest—the jet location in this case. In general, most of the grid points were clustered in the boundary layer, fins, jet, and the wake regions. The boundary spacing was selected to achieve a y+ value of 1.0.

The full grid for the finned projectile consists of multiple blocks for ease of mesh generation and grid clustering. The overall structured mesh consists of approximately 21.5 million hexahedral

cells (see figure 4). Separate blocks were used to mesh the inside of the nozzles with approximately 350,000 cells for each nozzle block. Another set of blocks was used to mesh the region containing the jet exit and the outer boundary. Figure 5 shows an expanded view of the surface mesh in the vicinity of a jet exit. It shows the clustering and a large number of grid points used axially in the entire jet interaction areas both upstream and downstream of the jet exit. Figure 6 shows a longitudinal cross section of the mesh containing two jets. This figure also shows the fine mesh used inside of the nozzle. Flow is computed inside of the nozzles. When a jet is activated, the time-dependent jet boundary condition is used at the bottom wall of the nozzle and total pressure and total temperature of the pulsed jet are imposed.

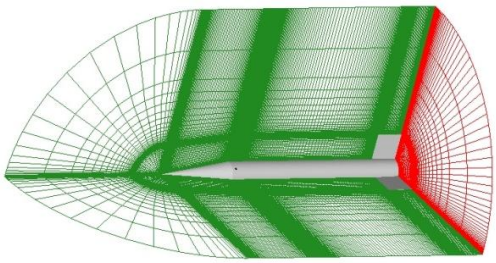

Figure 4. Full computational mesh for the finned projectile.

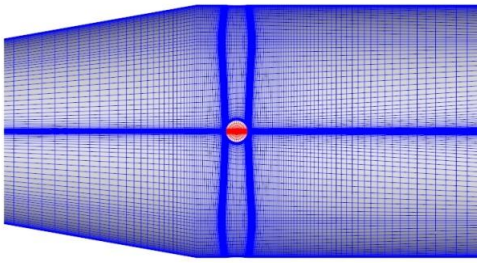

Figure 5. Expanded view of the surface mesh near the jet.

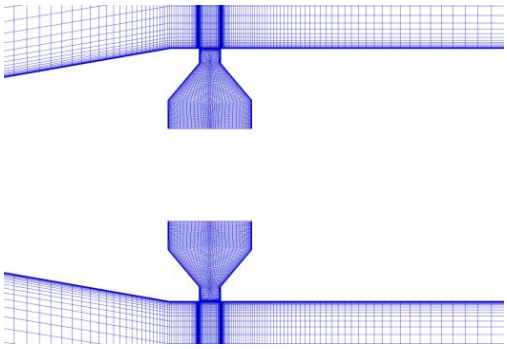

Figure 6. Computational grid for the nozzle jet.

4. Results

Both steady-state and time-accurate coupled CFD/RBD computations were performed using full 3-D Navier-Stokes computational technique, and no symmetry was used. Computed results obtained from steady-state CFD solutions were used in the aerodynamic model/RBD simulations described in section 2.6. Comparisons of the coupled results have been made with the results obtained with the aerodynamic model/RBD flight simulations.

4.1 Steady-State CFD Solutions

Before running fully coupled time-accurate CFD/RBD computations, some steady-state CFD computations were first performed for the basic finner configuration both with and without jet interaction at M = 2.0, 2.5 and $\alpha = 0°, 2°$. Solutions were obtained for these flow conditions and the effect of some CFD parameters was determined. Figures 7 and 8 show the computed normal force coefficient slope and the pitching moment coefficient slope, respectively, as a function of Mach number. Computed results are also compared with free flight data (*34*) for the same configuration for the jet-off conditions. Both the normal force and the pitching moment slopes match very well with the data. Both computed results and the data show a small decrease in the normal force coefficient and a small increase in the pitching moment coefficient with increase in Mach number from M = 2 to 2.5.

Computed results for the jet-on conditions were obtained with a steady normal jet interacting with the free-stream flow. Initially, a jet total pressure (P_0) of 34.5 MPa and a jet total temperature (T_0) of 2700 K were imposed at the nozzle inlet. These jet conditions are the same ones used in prior studies (*26, 27*). A quantity of primary interest was the jet thrust. Tables 1 and 2 show the calculated jet thrust results for different Mach numbers, angles of attack, and turbulence variables. These tables also show the forces on the jet wall and the jet inlet and the calculated jet thrust in the normal direction. The calculated jet thrust is 215 N and, as expected for constant jet pressure ratio, is practically the same for both Mach numbers, M = 2.0 and 2.5, and both angles of attack, $\alpha = 0°, 2°$ (see table 1). The effect of initial turbulence variables on the calculated thrust is also negligible (see table 2).

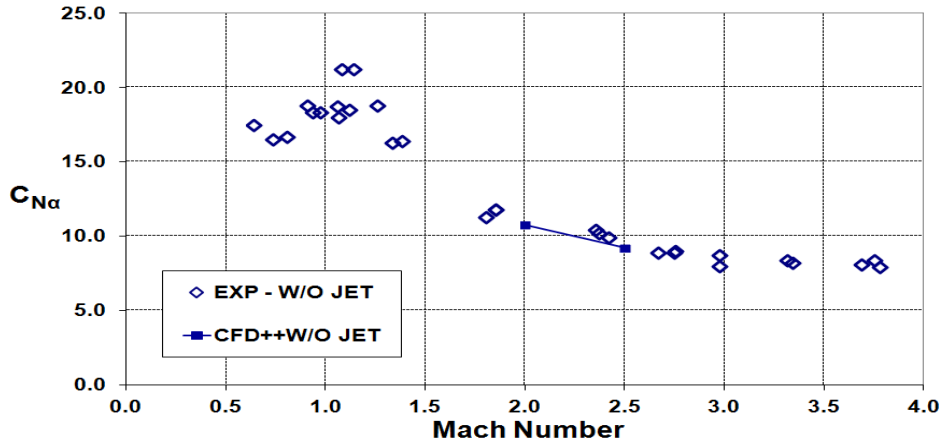

Figure 7. Normal force coefficient slope as a function of Mach number.

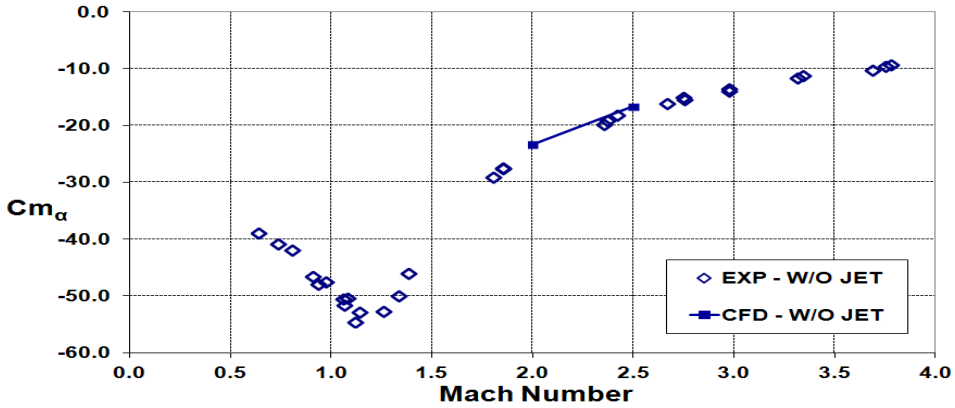

Figure 8. Pitching moment coefficient slope as a function of Mach number.

Table 1. Effect of Mach and angle of attack on jet thrust.

Mach Number	Angle of Attack	Jet Inlet Fz (N)	Jet Wall Fz (N)	Thrust (N) Jet Inlet + Jet Wall
2.0	0	–2691.57	2476.31	215.27
2.0	2	–2691.67	2476.31	215.36
2.5	0	–2691.57	2476.31	215.27
2.5	2	–2691.57	2476.31	215.27

Table 2. Effect of turbulence variables on jet thrust.

Turbulent Kinetic Energy (k)	Turbulent Dissipation Rate (∈)	Jet Inlet Fz (N)	Jet Wall Fz (N)	Thrust (N) Jet Inlet + Jet Wall
0.0	0.0	–2691.57	2476.31	215.27
2.77	941.78	–2691.57	2476.33	215.24

Steady-state jet computations were also performed at a higher jet pressure, P_0 = 345MPa. Computed results for both of these jet pressure cases are shown in table 3. These results show the angle of dependence of the force amplification factor, K_f, and the moment amplification factor, K_m, for the jet. The amplification factor is a measure of the efficiency of the jet or the jet interaction effect on the jet control force/moment. An amplification factor less than 1.0 indicates that the jet interaction effect decreases the effectiveness of the jet force (thrust)/moment. For the low-pressure jet (P_0 = 34.5 MPa) case, one can observe a decrease in the force amplification factor and an increase in the moment amplification factor as angle of attack is increased from 0° to 10°. The reverse trend is seen for angles of attack larger than 10°. The effect of angle of attack is rather small for the high-pressure jet case. These amplification factor results are needed as inputs into the aerodynamic model/RBD analysis and its comparison with the coupled CFD/RBD jet maneuver results.

Table 3. Effect of angle of attack on the jet amplification factors.

Angle of Attack (α)	**Jet (P_0 = 34.5 MPa, T_0 = 2700 K)**		**Jet (P_0 = 345 MPa, T_0 = 2700 K)**	
	K_f	**K_m**	**K_f**	**K_m**
0	0.803	1.092	0.944	1.099
2	0.772	1.079	0.935	1.077
6	0.678	1.111	0.923	1.070
10	0.617	1.221	0.921	1.086
12	0.653	1.199	—	—
15	0.807	1.119	—	—

4.2 Time-Accurate Coupled CFD/RBD Solutions

Time-accurate, unsteady numerical computations were performed using coupled Navier-Stokes CFD/RBD methods to predict the time-dependent response of a finned projectile subject to a jet maneuver at a supersonic speed, M = 2. Unsteady aerodynamics and flight dynamics were computed simultaneously. In all cases again, time-accurate solutions were obtained that required full 3-D computations and no symmetry was used. The primary interest is in the application of coupled CFD/RBD techniques for accurate simulation of the free-flight aerodynamics and flight dynamics of a projectile with a jet maneuver. Comparisons of the coupled results have been made with the results obtained with the aerodynamic model/RBD flight simulations described in section 2.6.

A variety of initial conditions were considered in the flight simulations (see table 4). These initial conditions were devised to isolate the unsteady, coupled roll-pitch-yaw flight behavior of jet-controlled projectiles at moderate angle of attack and supersonic speed. One of these cases, initial pitch rate case, represents a pure pitching motion with an initial pitch rate of 30 rad/s and no jet.

Table 4. Initial conditions.

Condition	Initial Pitch Rate	No Initial Angular Rate	Initial Yaw Rate	Initial Low Roll Rate	Initial High Roll Rate
Angular velocity (p, q, r), [rad/s]	(0, 30, 0)	(0, 0, 0)	(0, 0, 7)	(12.566, 0, 0)	(188.496, 0, 0)
Translational velocity (u, v, w), [m/s]	(680, 0, 0)	(680, 0, 0)	(680, 0, 0)	(680, 0, 0)	(680, 0, 0)
Attitude (ϕ, θ, ψ), [rad]	(0, 0, 0)	(0, 0, 0)	(0, 0, 0)	(0, 0, 0)	(0, 0, 0)
Position (x, y, z), [m]	(0, 0, 0)	(0, 0, 0)	(0, 0, 0)	(0, 0, 0)	(0, 0, 0)

For each of these cases, an appropriate starting CFD solution was obtained before running the coupled CFD/RBD computation. First, a computation was performed in the steady-state mode corresponding to the forward velocity of 680 m/s. The next step required time-accurate solutions in the uncoupled mode. For nonspinning cases (initial pitch rate, no initial angular rate, and initial yaw rate), computations were carried out in a time-accurate manner. For these cases, the solutions converged in a few hundred time steps. The initialization computations were also performed for the two spinning cases (initial low roll and initial high roll) in a time-accurate manner until mean values of the forces and moments converged. In the present calculations, one spin cycle was found to be adequate. For each roll rate case, 720 time steps were used for one spin cycle, which corresponds to the projectile rolling 0.5° every time step. This corresponds to a time step of 6.9444e-04 and 4.62962e-5 s for the low roll and the high roll cases, respectively, for these uncoupled calculations for the jet-off conditions. The solution at the end of the first spin cycle formed the initial condition for the coupled virtual fly-out simulation. In all five cases, time was set to zero at the beginning of the coupled calculations.

A pulse jet was activated only once at the beginning of the coupled simulations for the four jet cases (no initial angular rate, initial yaw rate, initial low roll rate, and initial high roll rate). The nozzle jet in these four jet cases was located at 0° roll position with the jet exit pointing downward in the positive z-direction. This was also the position at the start of the pulse jet for all cases with or without spin. The intent here is to activate the pulse jet in this orientation (jet on bottom) so that it kicks the projectile nose predominantly in the vertical plane. Some fixed-plane sideslip angle is often unavoidable due to the complex flight dynamics.

Different jet parameters as provided in table 5 were used in the simulations. A total impulse of about 4 N-s was considered for all four jet cases. A longer duration jet pulse was executed for three of these four sets of initial conditions: no initial angular rate, initial yaw rate, and initial low roll rate. A shorter duration jet pulse was used for the initial high roll rate case only. For the long duration case, the total impulse requires a thrust magnitude of 200 N for 20 ms. Similarly, we considered a thrust magnitude of 2000 N for 2 ms for the short duration case. The newly developed time-dependent jet boundary condition was imposed in the coupled simulations to

achieve the desired impulse. This required a peak in total pressure and total temperature of 34.5 MPa and 2700 K to be imposed for the long duration cases and a peak in total pressure and total temperature of 345 MPa and 2700 K for the short duration case. Again, these values for the long duration case are the same ones used in prior studies (*26*, *27*). The activation and deactivation of the pulse jets were done over a few time steps, i.e., gradually ramped up or down to avoid numerical issues.

Table 5. Jet conditions.

Condition	**Jet Interaction, Long Duration**	**Jet Interaction, Short Duration**
Total jet pressure, P_0 (MPa)	34.5	345
Total jet temperature, T_0 (K)	2700	2700
Jet duration (Δt_J), (ms)	20	2
Desired jet impulse (N-s)	4	4

The time steps for computations with the pulse jets were chosen to be small so as to capture the transient jet effects. Time steps of 6.9444e-05 and 4.62962e-5 s were used for the low roll case and the high roll case, respectively. The time steps chosen may not be small enough to fully resolve the transients associated with the jet turning on and off but are believed to be sufficient to address the transients associated with the interaction between the jet and the projectile dynamics. A time step of 2.0e-05 s was used for other jet-on cases with no roll. To achieve even better time accuracy, 40 inner time iterations were used in some cases in the beginning during the transient jet interaction phase of the calculations. The number of inner iterations was subsequently reduced to 20 for later times when the jet interaction effects were no longer present. The actual peak jet thrust obtained from the calculations was 215 N for the long duration case and approximately 10 times larger for the short duration case.

For comparison of the coupled CFD/RBD results, aerodynamic (or aero) model/RBD flight simulations (see section 2.6) were also conducted for each of these cases. As stated earlier, the basic aerodynamics used in the aero model/RBD analysis came from a previous study (*33*). The jet interaction effects on the force and moment applied to the projectile due to jet activation were derived from the present steady-state CFD computations (see table 3). The jet interaction data computed from our steady-state CFD results included both the force and the moment amplification factors over a range of angles of attack. Ideally, the full aerodynamics used in the aero model/RBD flight simulations should resemble as closely as possible the ones used in the coupled computations; however, some small differences may exist due to mesh and Reynolds number effects with the already available basic aerodynamics used here.

To summarize, a total of five cases were examined, each with unique initial and/or jet conditions. In some instances, multiple aerodynamic model/RBD simulations were conducted for each of these cases to isolate phenomena such as jet interaction.

Some qualitative results of the coupled simulations are now presented. Even though there are five cases considered (see table 4), three cases use the longer duration jet pulse (same total jet pressure and temperature) and, therefore, qualitative features of the flow fields are expected to be similar for these three cases. We have chosen the initial low roll rate case to be representative of the three cases. In addition, qualitative results obtained from the coupled simulations for the initial high roll rate case are also shown and compared with initial low roll rate case. Figure 9 shows the computed pressure contours near the projectile during the peak of the pulse jet at an initial Mach = 2.0 case for both the initial low and high roll rate cases. The computed pressure contours in both cases clearly show the jet interaction flow field in the xz plane at the bottom of the projectile. The orientation of the projectile changes from one instant in time to another as the projectile flies forward to the right. One can begin to see the attitude of the projectile change after the jet has been activated for the low roll case. In both cases, the computed pressure contours show the high-pressure region in front of the jet (shown in red) and low pressure downstream of the jet (shown in blue), and the complex jet-interaction flow structure, as expected. In addition, the jet interaction region both upstream and downstream of the jet location is much larger for the high roll case with the stronger pulse jet compared to the low roll case with the weaker jet. As expected, during the turning on (activation) and turning off (deactivation) of the pulse jet, the jet interaction flow field is time-dependent.

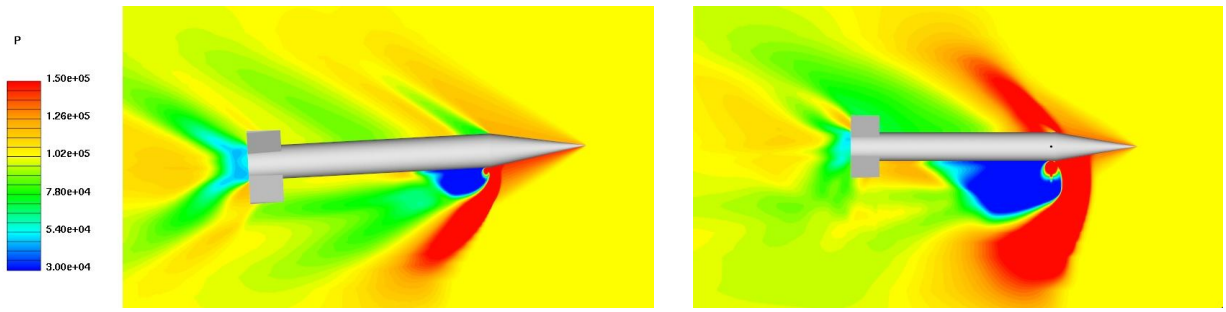

Figure 9. Computed pressure contours at jet peak: low roll (left) and high roll (right).

The time-dependent jet interaction flow fields for the low initial roll rate case are shown in figure 10, with 10a showing the computed pressure contours for the ramping of the jet-on period, and 10b showing the computed pressure contours during the ramping down of the pulse jet. As shown in figure 10a (from top to bottom), the jet interacts more into the incoming free stream with the jet interaction shock becoming stronger and the low-pressure region behind the jet becoming larger (seen in blue). When the jet is off, as seen with the top picture in figure 10a, the flow field is symmetric. Once the jet peak pressure is reached, the jet stays on at the peak pressure for 20 ms in this low roll case. Clearly, in figure 10b, the angle of attack of the projectile has changed considerably before the ramping down of the pulse jet. Again, looking at figure 10b from top to bottom, the jet interaction flow field and, especially, the low-pressure region downstream of the jet (shown in blue) becomes smaller and smaller until it vanishes approximately 5 ms after the jet is turned off. The corresponding flow field is shown in the bottom picture of figure 10b, which essentially is the flow field of the projectile at an angle of attack.

Similar time-dependent jet interaction flow field results for the high initial roll rate case are shown in figure 11. Figure 11a shows the computed pressure contours during the jet activation starting just after the jet activation. The jet interaction regions both upstream and downstream of the jet location continually increase until the jet peak is reached. The reverse is true when the pulse jet is ramped down or deactivated (see figure 11b). Because of the short duration of the pulse jet in the high initial roll rate case, the flight dynamic response is not fast enough, and the change in the attitude of the projectile is found to be minimal even during the jet deactivation period.

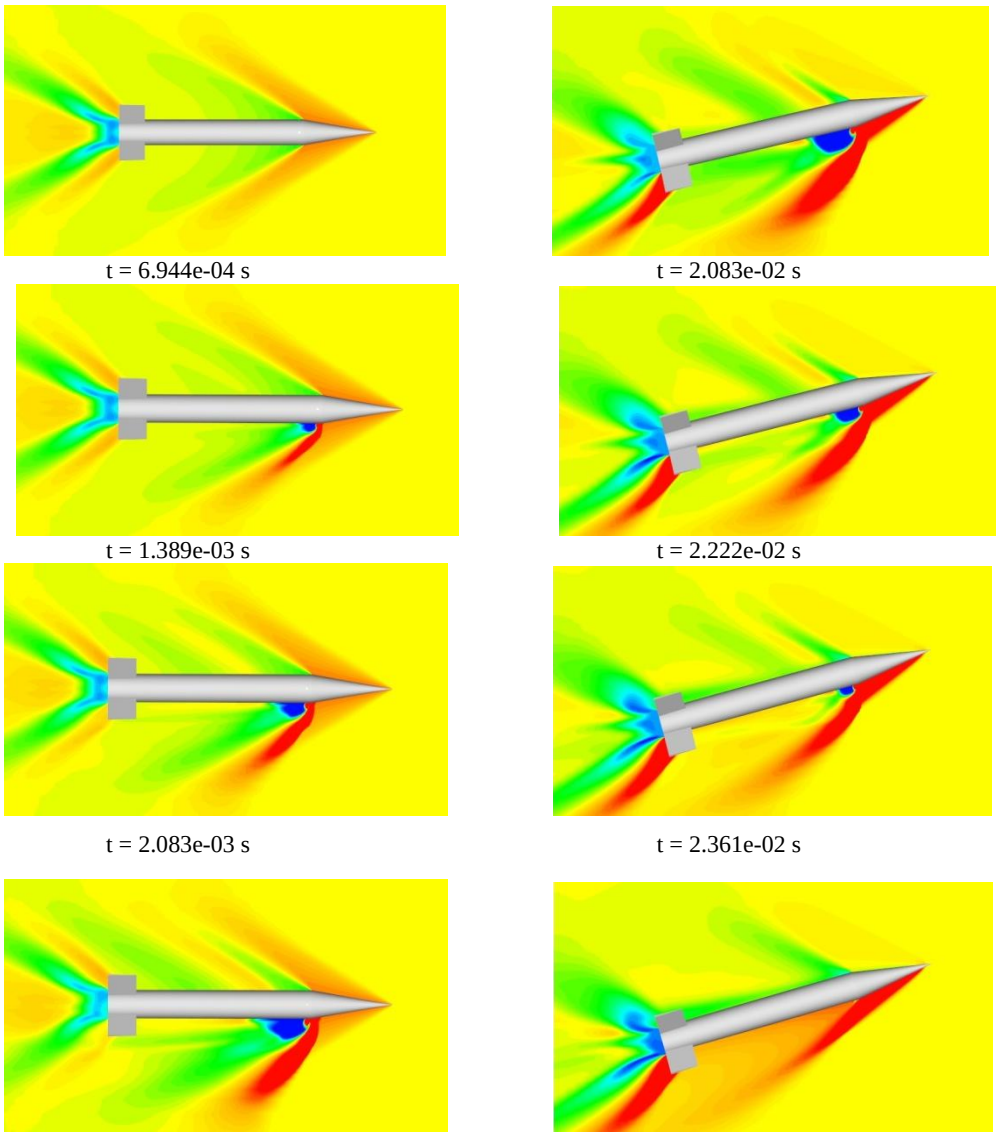

Figure 10. Computed pressure contours for the low roll case during (a) jet-on and (b) jet-off for the pulse jet.

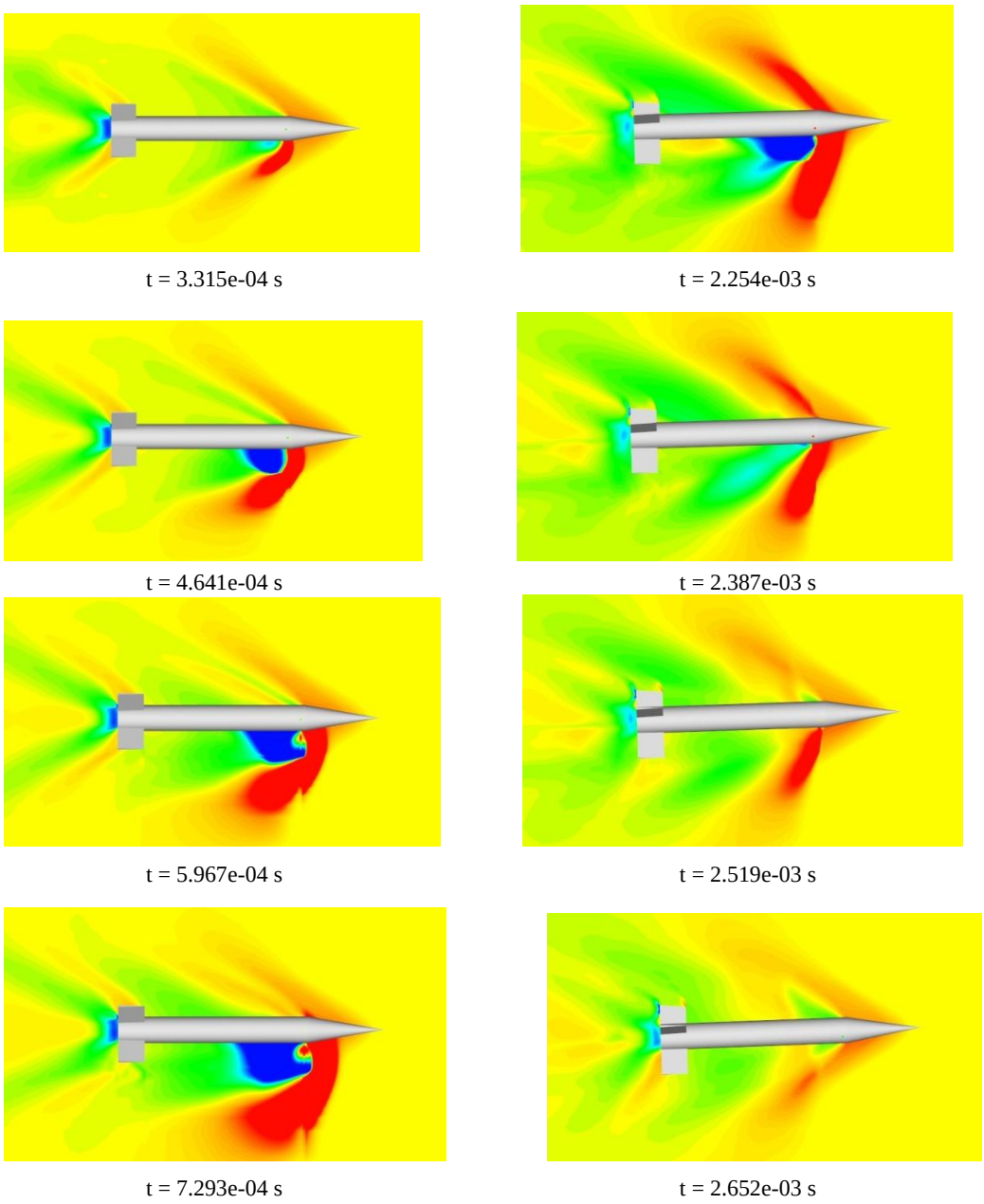

Figure 11. Computed pressure contours for the high roll case during (a) jet-on and (b) jet-off for the pulse jet.

4.3 Comparison of Coupled CFD/RBD Results With Aerodynamic Model/RBD Simulations

Flight simulations were conducted to compare the two aerodynamics assessment methods (aero model/RBD and coupled CFD/RBD) without the jet. The flight was given an initial pitch rate of 30 rad/s and a forward velocity of 680 m/s and the jet was not activated. Figure 12 provides metrics for the angular motion of the projectile. The fixed-plane y moment oscillates and the fixed-plane z moment and fixed-plane sideslip angle is zero since the projectile undergoes purely pitching motion and the roll rate is zero. This initial pitch rate produces a maximum total angle of attack of about 14°. Total angle of attack is slightly (less than 1°) higher for the aero model/RBD method than the coupled CFD/RBD method. Very small differences in the fixed-plane y moment and resulting differences in the total angle of attack highlight small differences in the pitching moment. Projectile linear theory (*32*) attributes the natural frequency of the angular motion mostly to the pitching moment. Likewise, the amplitude and damping of angular motion is driven by pitch damping moment and side moments (such as Magnus) (*32*).

Inspection of figure 13 permits comparison of drag between methods. The axial force illustrates differences in the zero-yaw drag. At higher total angle of attack, the results indicate nonlinearity. The differences in axial force (approximately 10%) are consistent with minor differences in Mach number over the short flight.

Evaluation of lateral forces enables some comparison of the swerving motion (see figure 14). The normal force magnitude is almost the same between the aero model/RBD method and the coupled method. Very small differences in angular motion and normal forces yield negligible differences in the trajectory (less than a 0.1-m difference in cross range at 70 m downrange).

This comparison of methods for a simple initial pitch rate provides some expectation for general level of agreement between methods when examining jet control cases. Very small differences in the methods may be attributed to meshing, turbulence modeling, aerodynamic coefficient errors, or aerodynamic modeling deficiencies. The aerodynamics input to the aero model/RBD method came from different sources so there are differences in the aerodynamics used in the two methods. Further research may be needed to isolate and quantify reasons the small differences in the aerodynamics between the methods. Ideally, the aerodynamics input should be the same for both methods.

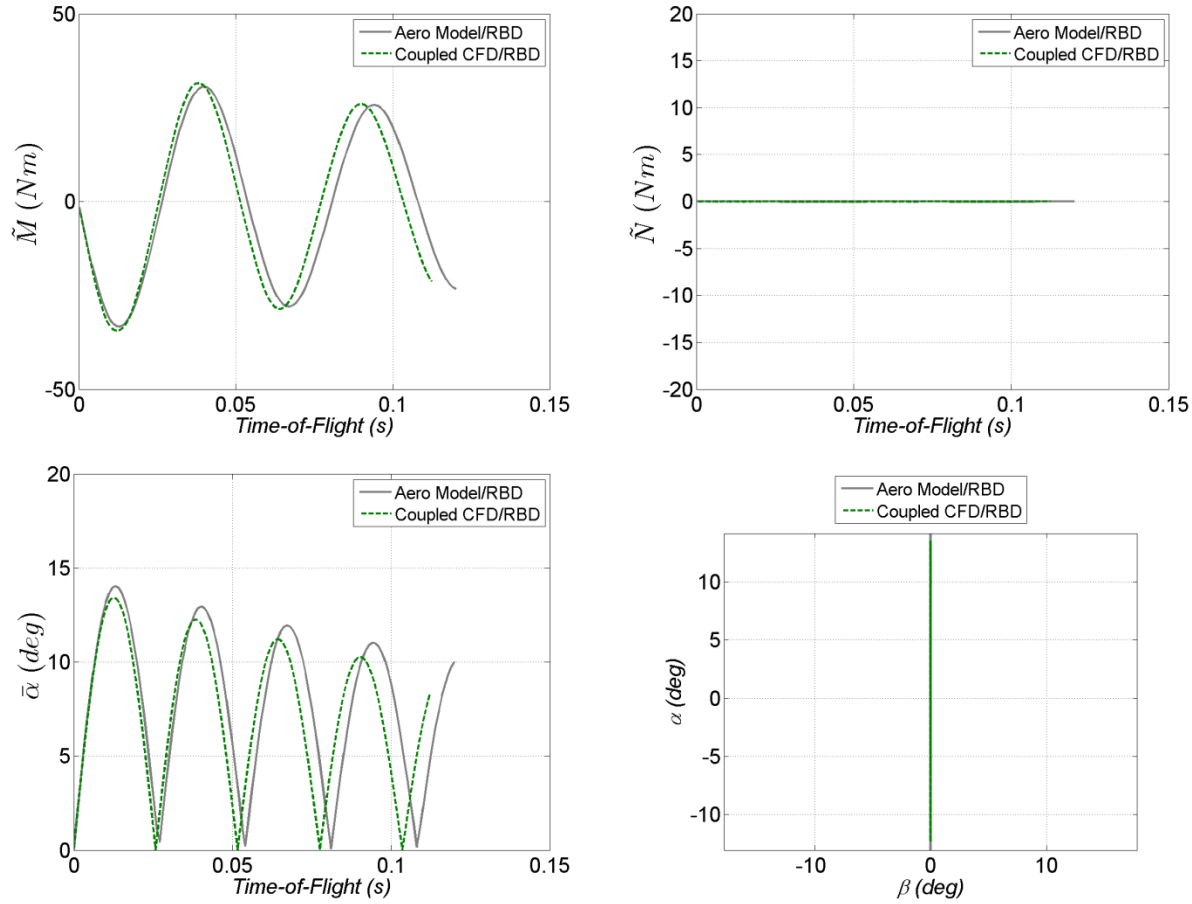

Figure 12. Angular motion metrics for initial pitch rate with no jet.

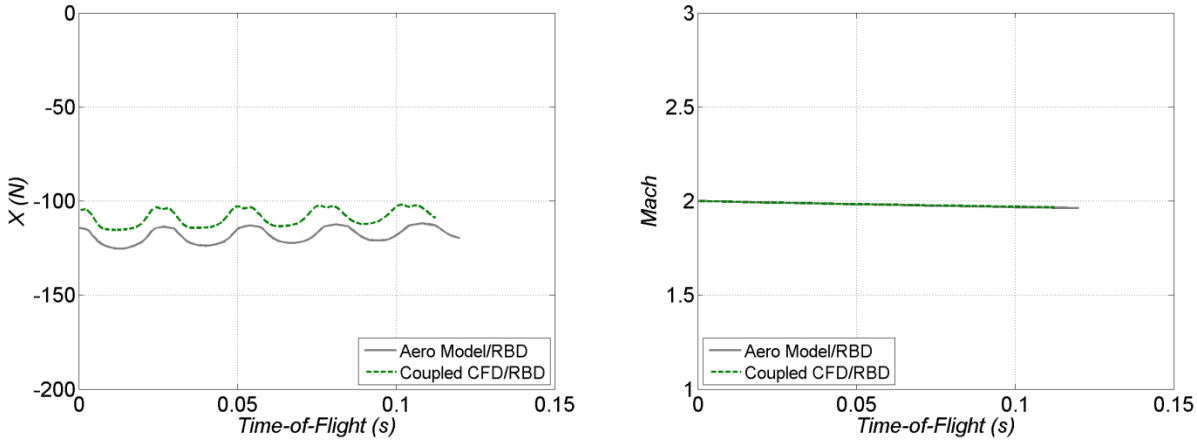

Figure 13. Axial motion metrics for initial pitch rate with no jet.

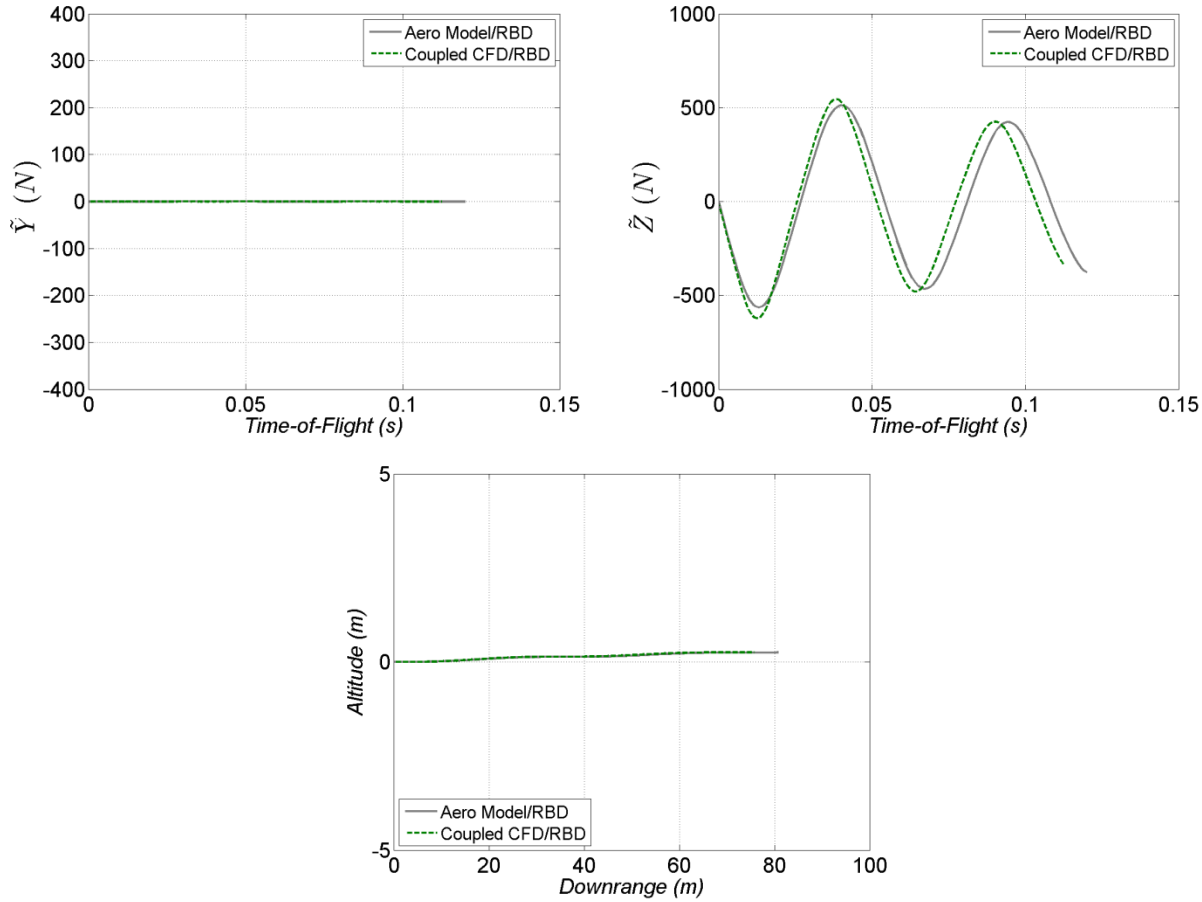

Figure 14. Lateral motion metrics for initial pitch rate with no jet.

The flight dynamic response of the finned projectile with the jet maneuver was examined and representative computed results obtained from the coupled virtual fly-out simulations are presented next. The coupled CFD/RBD simulations were also compared with results from the aerodynamic model/RBD method (*33*). Each flight metric (e.g., Mach, trajectory, angle of attack) is presented with a subplot for each case. All force, moment, and angle-of-attack data are expressed in fixed-plane coordinates using the transformation described previously in equation 9. Forces and moments are combined aerodynamic and jet contributions. Again, as shown in the previous section, there are some minor differences in the baseline (jet-off) aerodynamics used as input to the aerodynamic model/RBD method and those predicted by the coupled CFD/RBD method. Also, the jet interaction effects were included in the aerodynamic model/RBD using the jet force and amplification factors in two ways, first with 0° angle-of-attack values only and then adding the angle-of-attack dependent values.

First, the roll dynamics are investigated. The fixed-plane x (combined aerodynamic and jet) moments, roll rate, and roll angle histories are shown in figures 15, 16, and 17, respectively. Inspecting the fixed-plane x moment for the no initial angular rate case illustrates very low roll moment (less than 0.01 N-m). The jet issues in the pitch plane and there is no tip-off (initial pitch

and yaw angular rate) or initial roll rate to produce significant static roll moment or roll damping. The roll rate response for the no initial angular rate case in figure 16a shows a small roll rate (peaking around 0.5 Hz), which may be due to asymmetries in the jet or some numerical noise possibly attributable to grid density, symmetry arguments, and integrating almost equal pressure distributions on the body to yield the x moment that partially dictates the roll behavior. At 0° angle of attack, roll dynamics are inherently unstable since a very small roll moment one way or the other rolls the projectile from rest. For this reason, it is not unreasonable for small numerical noise to yield nonzero roll rates, and this behavior provides some measure of numerical uncertainty of the results in roll. The aerodynamic model/RBD simulation predicts zero roll moment and roll rate. As seen in these figures, both aerodynamic model/RBD simulations with jet interaction (using $\alpha = 0^o$ values and no angle-of-attack dependence) and α-dependent jet interaction are practically the same.

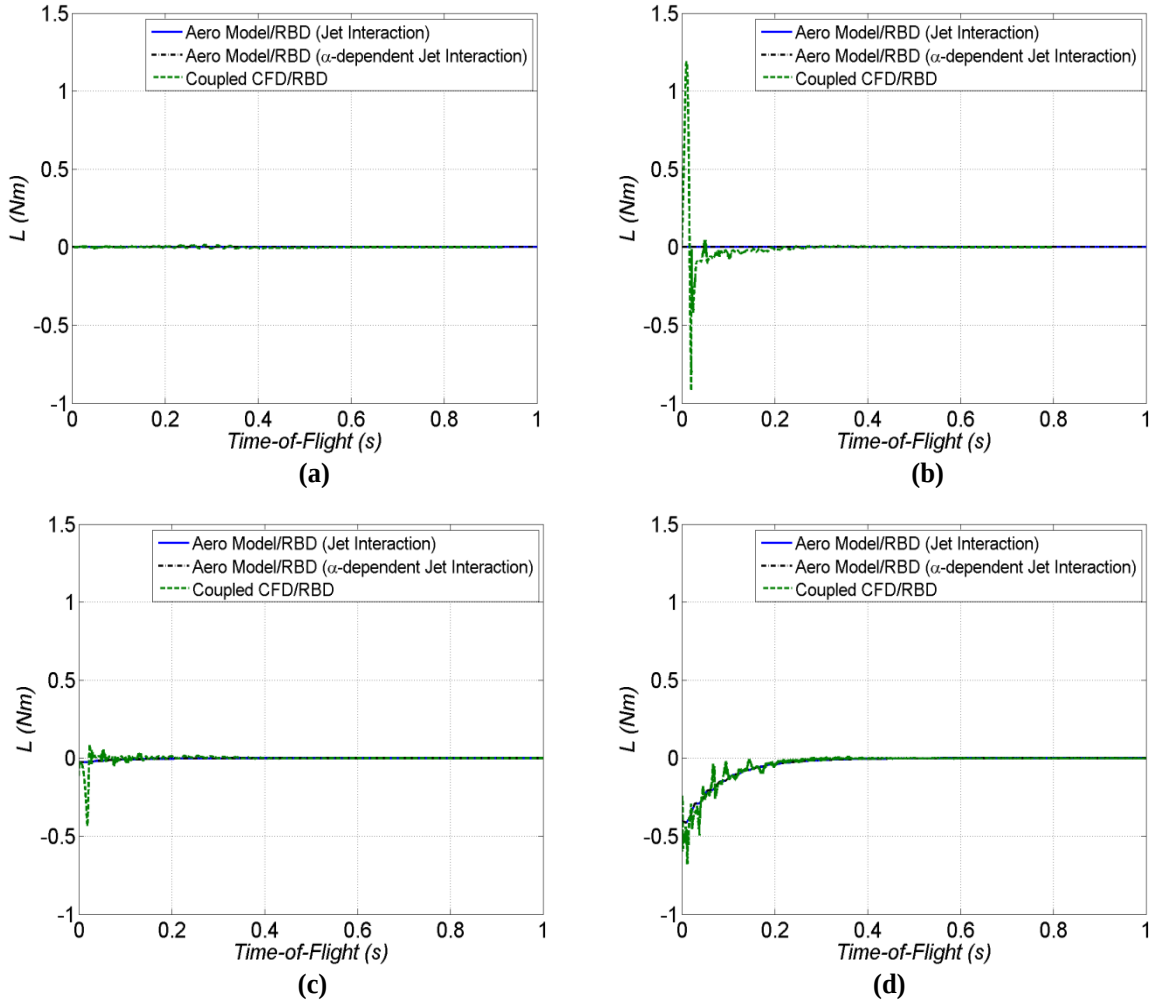

Figure 15. Time history of aerodynamic moment, ***L***: (a) no initial angular rate, (b) initial yaw rate, (c) initial low roll rate, and (d) initial high roll rate.

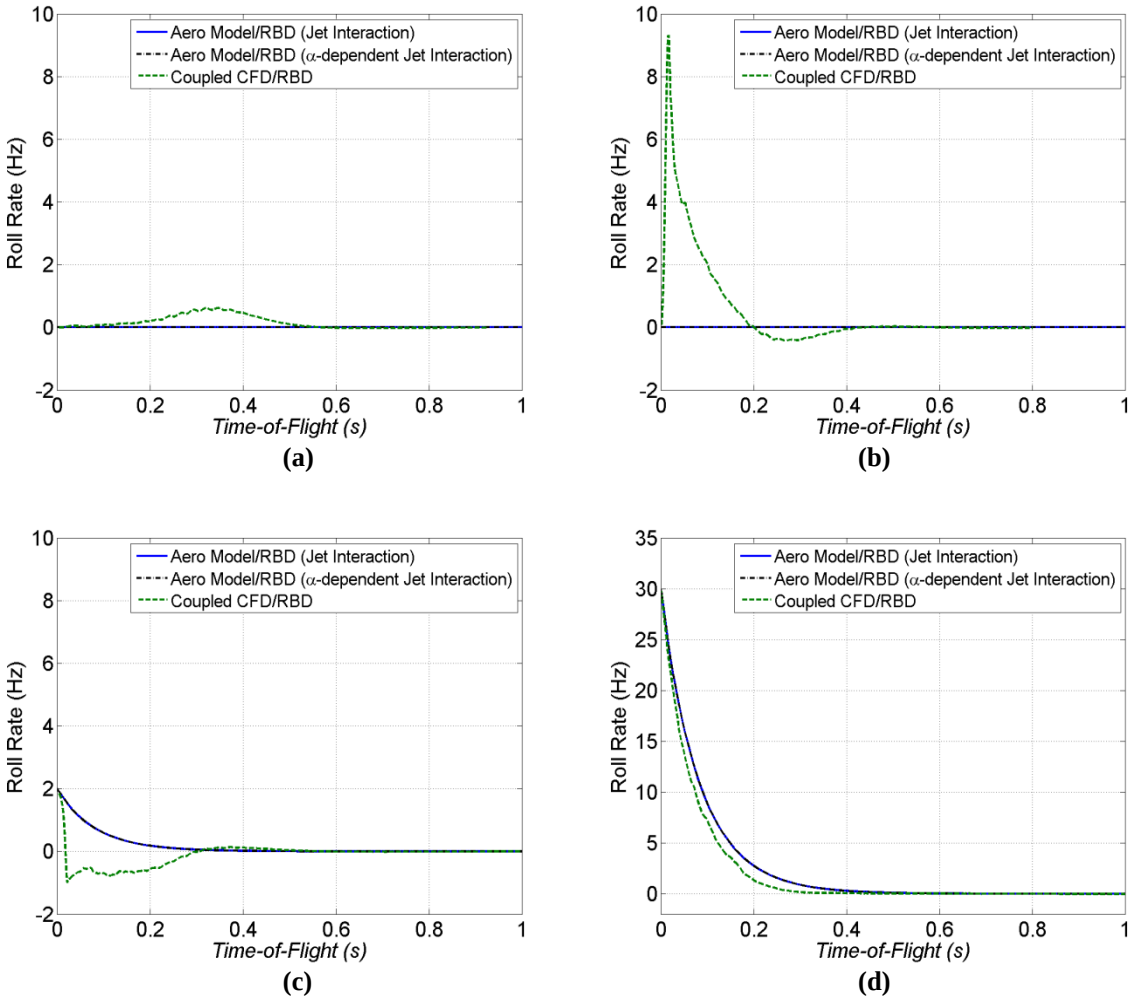

Figure 16. Roll rate vs. time: (a) no initial angular rate, (b) initial yaw rate, (c) initial low roll rate, and (d) initial high roll rate.

The roll dynamics for the initial yaw rate case demonstrates coupling between the roll, pitch, and yaw. The projectile is subject to an initial yaw rate (no initial roll or pitch rate) but the jet is activated in the pitch plane. As the jet ejects and sweeps over the body and fins undergoing yaw, a roll moment is produced. This roll moment, shown in figure 15b, is positive early in the jet event and becomes negative near 0.02 s due to the jet interaction effects. After the end of the jet, the roll response of the projectile is dictated by the roll damping moment from the induced rolling motion. The time scale for this change in the roll moment is about equivalent to the time period when the pulse jet was on. Clearly, this is a direct result of the jet interaction effects and highlights the unsteadiness of the problem. The roll moment for this case results in the roll rate seen in figure 16b. The asymmetric, unsteady flow over the fin due to the yawing motion (there is no yawing motion due to jet alone to be shown later in angular motion plots) and jet activation produces a significant roll rate (peaking to almost 10 Hz) that damps within about 0.4 s to zero. The corresponding roll data in figure 17b shows the roll angle changes about 160° over the flight. Over the time scale of the jet roll angle changes almost 40°, which alters the vectoring of

the jet for the lateral dynamics. The aerodynamic model/RBD flight simulation does not capture these effects; therefore, the roll moment and roll rate remain zero throughout the flight with jet maneuver.

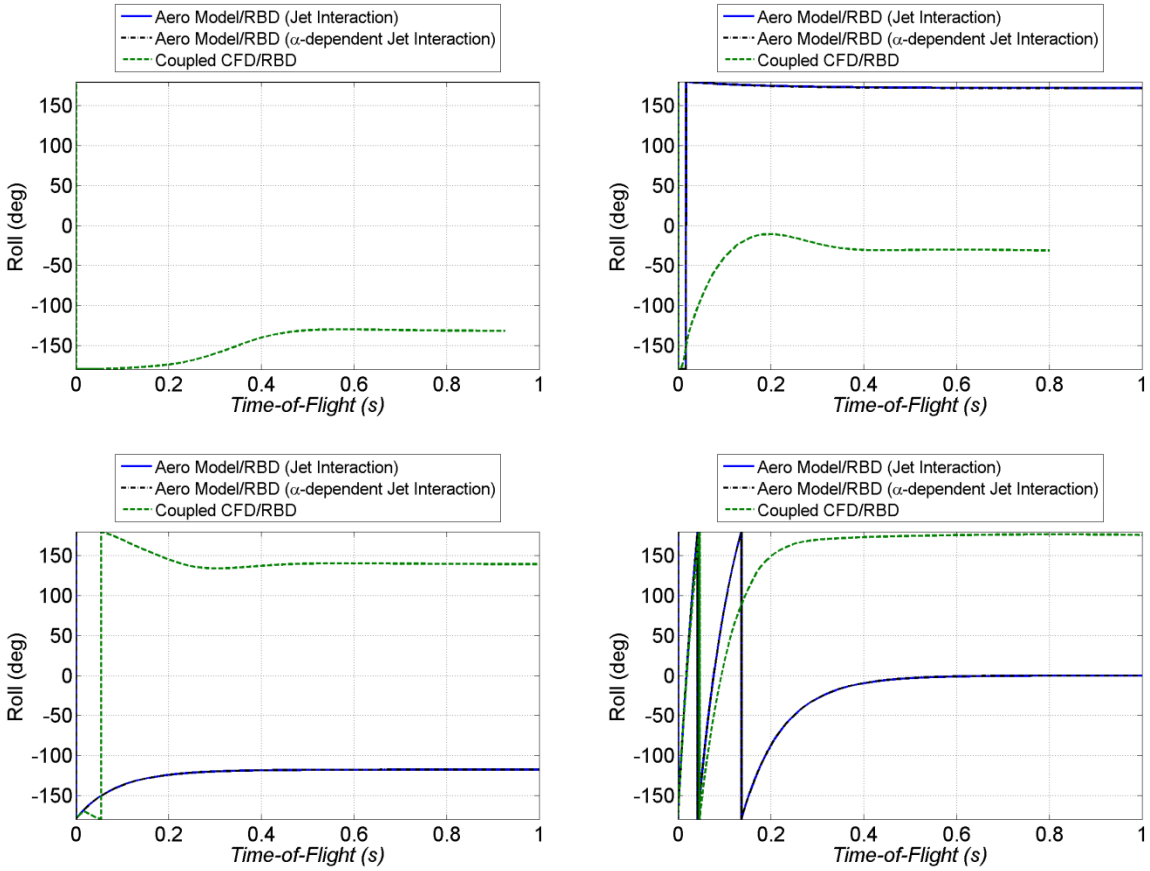

Figure 17. Roll vs. time: (a) no initial angular rate, (b) initial yaw rate, (c) initial low roll rate, and (d) initial high roll rate.

Unsteadiness and roll, pitch, yaw coupling are also evident for the roll dynamics of the initial low roll rate case. The net product is still a rapidly changing roll moment over the time scale of the jet due to the flow asymmetry of the four fins in the jet disturbance and wake of the projectile at angle of attack. The jet induces the projectile to an angle of attack. The roll moment varies with aerodynamic roll angle and total angle of attack, which leads to oscillation in the roll moment to slightly positive and negative values over approximately the first 0.4 s (total angle of attack varies from 5° to 15° for these times, to be shown later). The roll rate history in figure 16c features very small oscillations that damp to zero within about 0.4 s. The aerodynamic model/RBD (with or without angle-of-attack dependencies in jet control) simulation does not contain these complex elements; only the roll damping is incorporated.

As the roll rate increases and the jet activation time decreases, the effect of unsteady and coupled roll, pitch, and yaw phenomena on the flight dynamics is reduced. The roll moment for the high initial roll rate case is dominated by roll damping. The complex flow structures and asymmetric pressure distributions on fins are still present but the higher roll rate effectively “rolls out” the unsteady, asymmetric effects. Roll rate response for the coupled CFD/RBD simulations decreases from about 30 Hz to about zero within about 0.4 s. The aerodynamic model/RBD simulations with jet interaction match the coupled CFD/RBD simulation to within about 1 Hz over all times investigated (see figure 16d). These differences in roll rate produce the different roll angles in figure 17d. Differences between the coupled CFD/RBD and aerodynamic model/RBD roll dynamics may be attributable to differences in the roll damping moment input in the aerodynamic model/RBD and those predicted by the coupled CFD/RBD simulation.

Examination of the lateral moment histories that dictate the angular response provides further physical understanding. The fixed-plane y and z combined aerodynamic and jet moments are provided in figures 18 and 19, respectively. The jet moment is mainly in the fixed-plane y direction (some bleeds over into the z direction for results that have nonzero roll rate since the jet is on for a finite duration and is attached to the body that rotates about the roll axis) and induces angle of attack in the body, which causes the pitching moment to contribute to the total fixed-plane y moment. The lateral moment magnitude decreases with decreasing angular motion amplitude. The actual amplitude predicted by the coupled method in the beginning is slightly higher than the value predicted by aerodynamic model/RBD. Comparison is better for the initial high roll rate case.

Fixed-plane angular motion histories are presented in figures 20 and 21. Most cases show a maximum total angle of attack over about 15°. The no initial angular rate case purely pitches with an angle of attack of about 2° lower for the aerodynamic model/RBD method than the coupled CFD/RBD simulations. This discrepancy is likely due to the transient jet interaction effects not captured in the aerodynamic model/RBD. The aero model/RBD angular motion results do not change appreciably with angle-of-attack-dependent jet control.

There is less agreement in angular motion between methods for the initial yaw rate case. The coupled simulation encountered coupling between the initial yaw rate and pitch-inducing jet due to asymmetric flow over fins that caused a rolling motion. This effect caused the jet to bleed over more into the yaw plane and rotated the angular motion off the vertical axis as seen for the coupled simulation results in figure 20b. Regardless, there is about 5° of maximum fixed-plane sideslip angle amplitude for the initial yaw rate case.

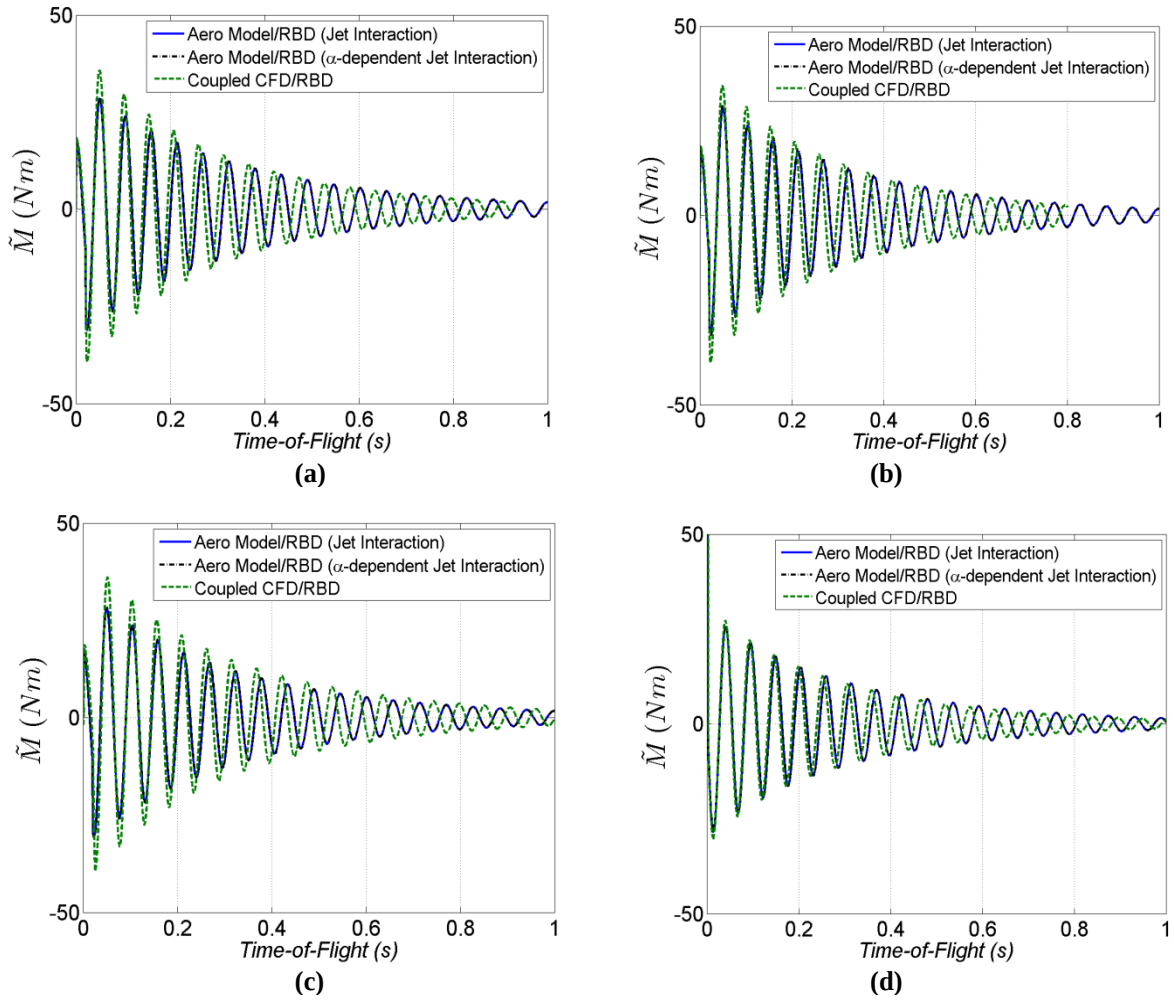

Figure 18. Time history of aerodynamic moment, $\tilde{\boldsymbol{M}}$: (a) no initial angular rate, (b) initial yaw rate, (c) initial low roll rate, and (d) initial high roll rate.

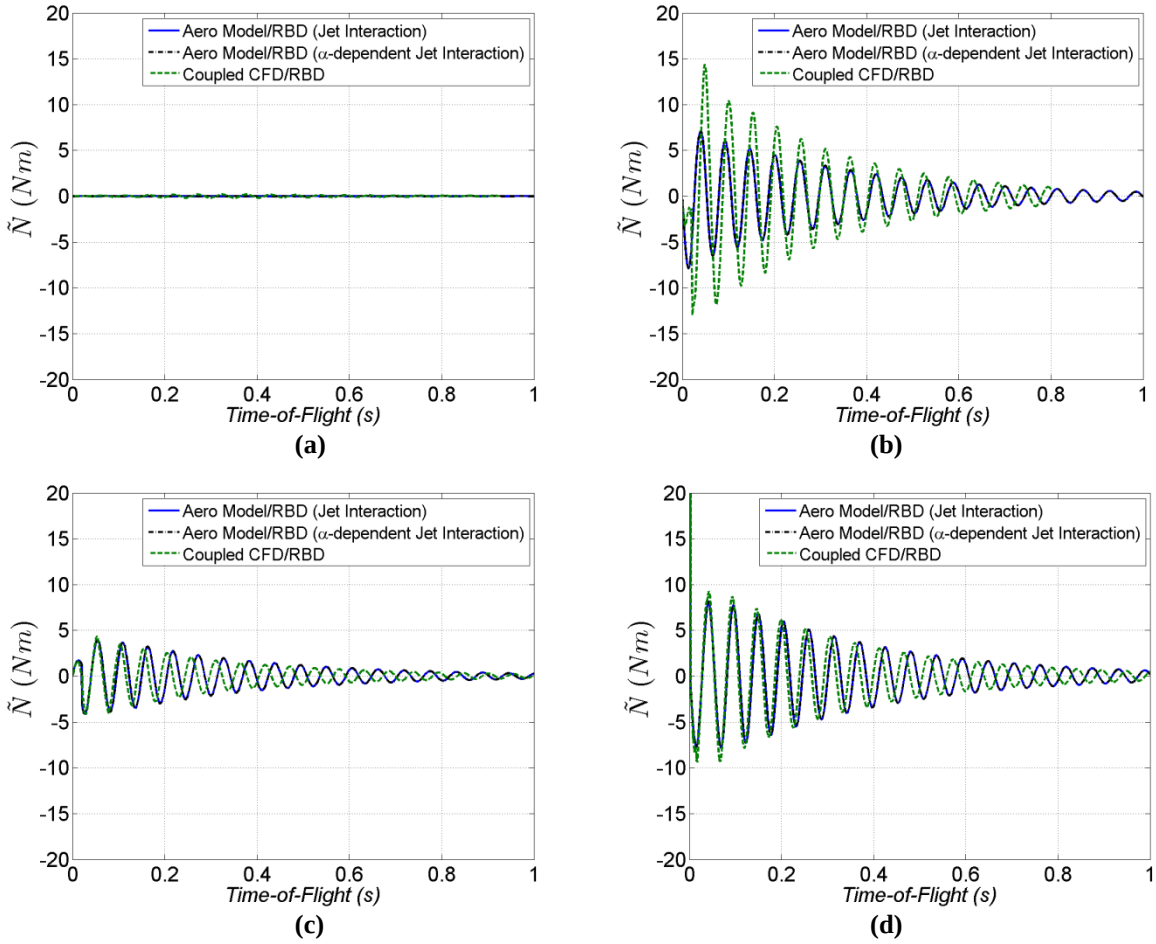

Figure 19. Time history of aerodynamic moment, $\tilde{\boldsymbol{N}}$: (a) no initial angular rate, (b) initial yaw rate, (c) initial low roll rate, and (d) initial high roll rate.

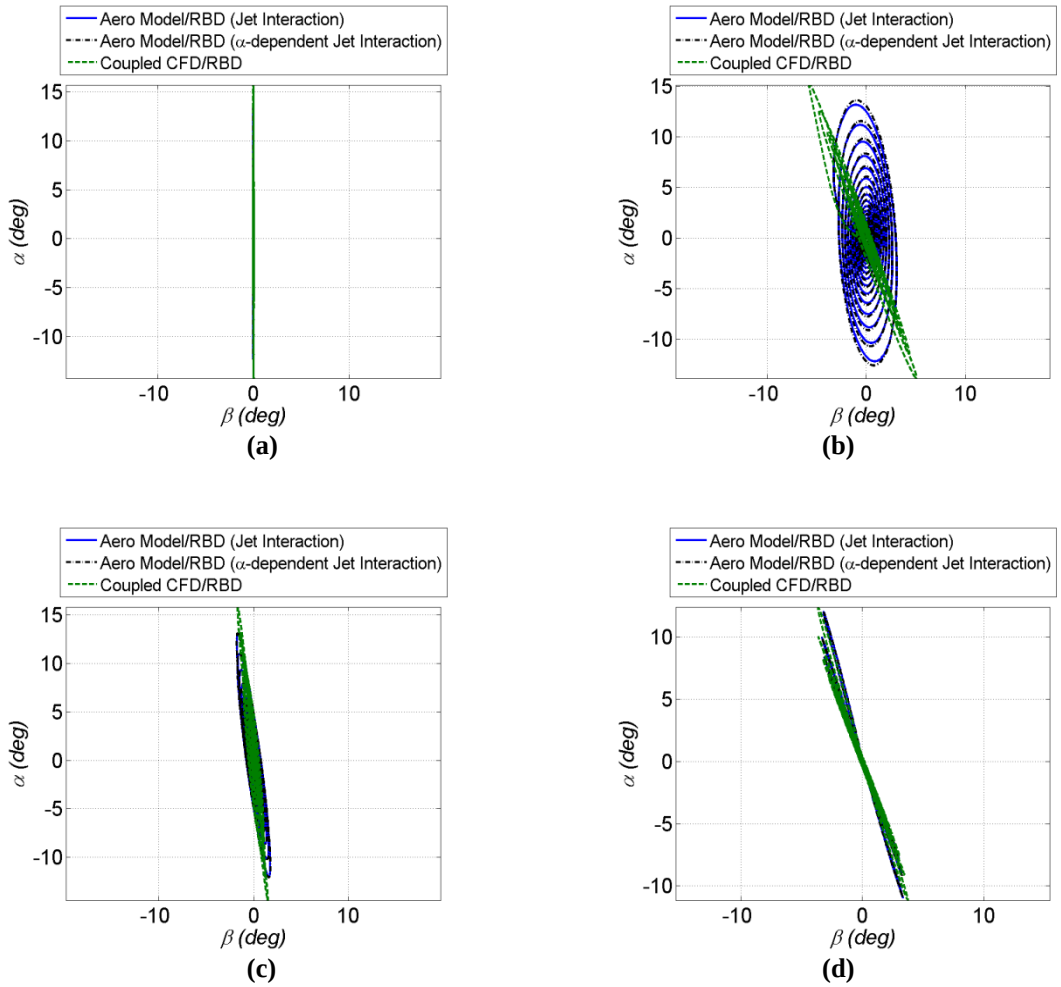

Figure 20. Angular motion: (a) no initial angular rate, (b) initial yaw rate, (c) initial low roll rate, and (d) initial high roll rate.

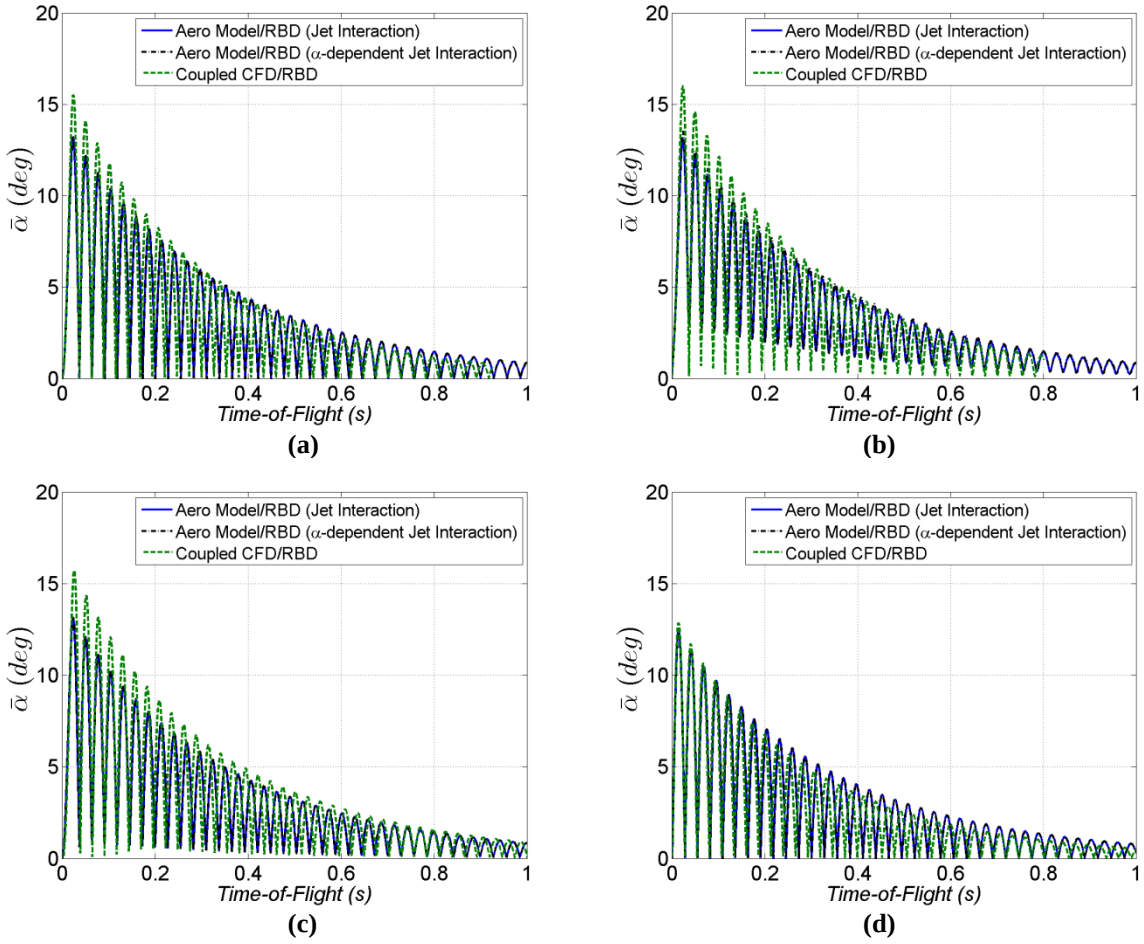

Figure 21. Total angle of attack vs. time: (a) no initial angular rate, (b) initial yaw rate, (c) initial low roll rate, and (d) initial high roll rate.

For both low and high initial roll rates, the projectile featured more pitching than yawing motion. The aerodynamic model/RBD simulations featured about 2° higher total angle of attack for the low initial roll rate case; however, the comparison is good (difference of less than 0.5°) for the initial high roll rate case. Overall results indicated agreement between the coupled CFD/RBD and aerodynamic model/RBD simulations to within about 3° total angle of attack.

The magnitudes of the axial forces are shown in figure 22. As expected, axial forces scale with total angle of attack. There is reasonable agreement in both zero-yaw and yaw-dependent axial forces between the coupled CFD/RBD and aerodynamic model/RBD simulations (as seen for the no jet case). The Mach number history is presented in figure 23. Here, we see the projectile slows down from M = 2 to almost M = 1.7 after 1 s time of flight. Specific details in the aerodynamics and angular motion produce minor differences in Mach histories between the two methods.

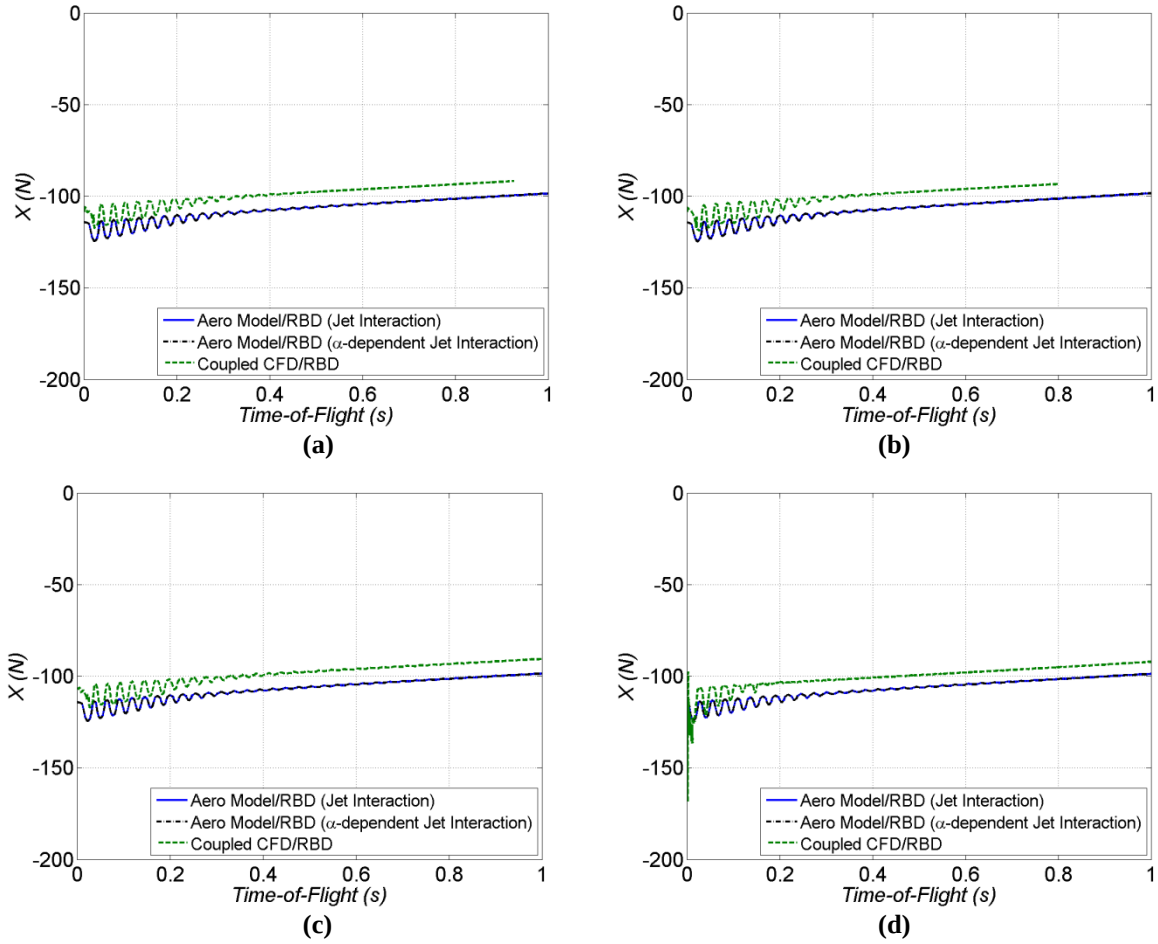

Figure 22. Time history of aerodynamic force, ***X***: (a) no initial angular rate, (b) initial yaw rate, (c) initial low roll rate, and (d) initial high roll rate.

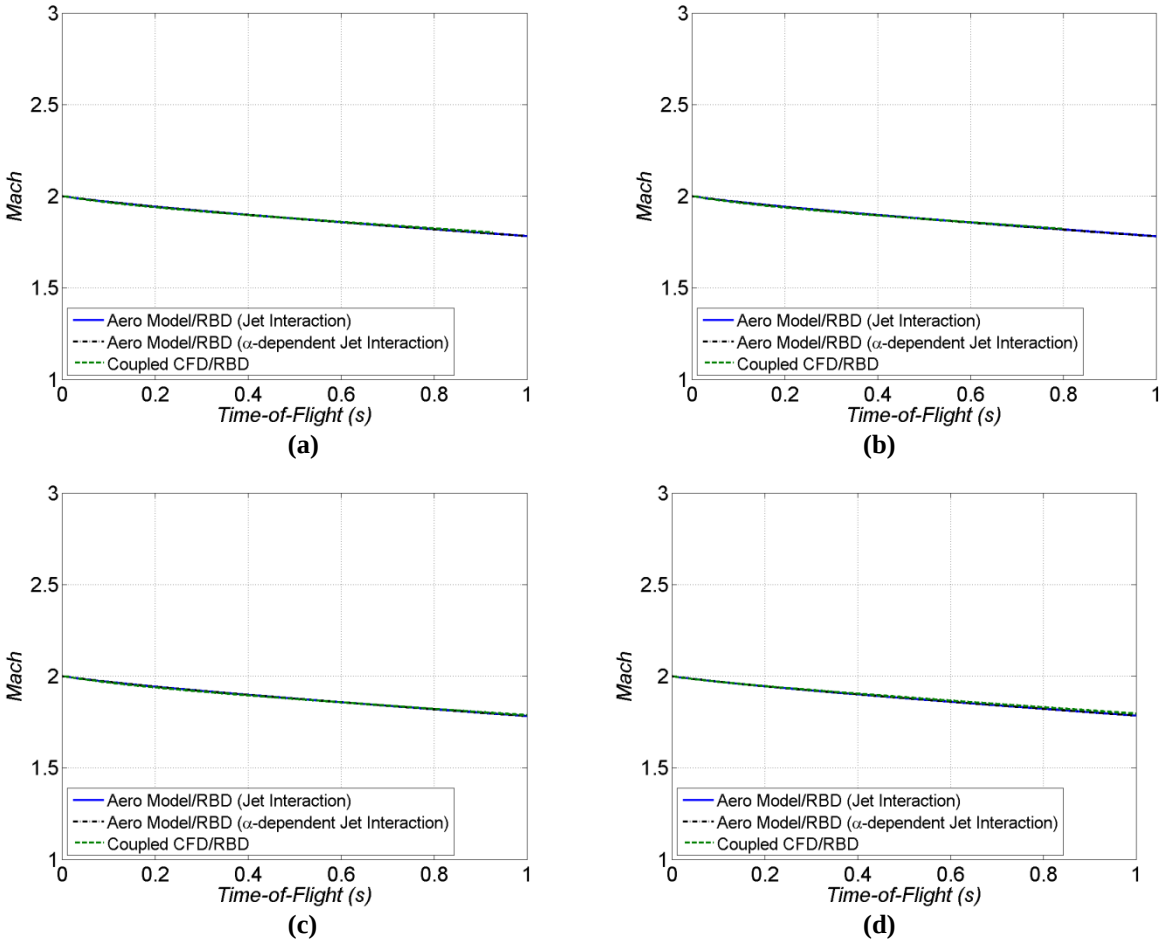

Figure 23. Mach number vs. time: (a) no initial angular rate, (b) initial yaw rate, (c) initial low roll rate, and (d) initial high roll rate.

Description of the combined aerodynamic and jet fixed-plane Y and Z forces in figures 24 and 25 is similar to earlier comments on the lateral moments and angular motion. The jet force is mainly in the z direction. Rolling induced by coupling with pitch/yaw vectors the jet thrust differently between methods for all cases but the no initial angular rate case. Generally good agreement is obtained between the two methods for the Y force for all cases except the initial yaw rate case. In that case, a much lower magnitude of the amplitude is seen with the aerodynamic model/RBD method (see figure 24b). Consistent with figure 21, initially larger Z forces are predicted by the coupled method compared with the aerodynamic model/RBD method in the no initial angular rate, initial yaw rate, and initial low roll rate cases. Agreement is somewhat better between the two methods for the initial high roll rate case.

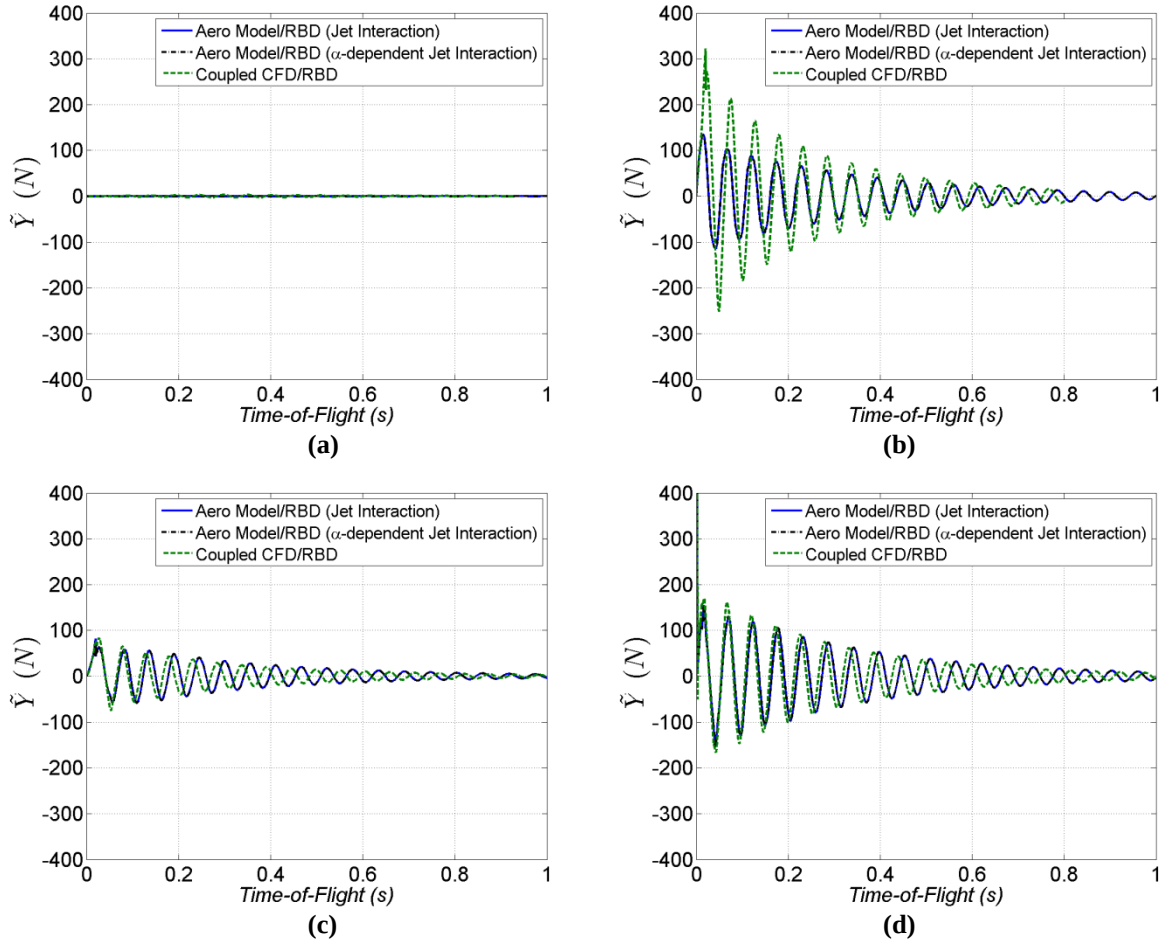

Figure 24. Time history of aerodynamic force, $\tilde{\boldsymbol{Y}}$: (a) no initial angular rate, (b) initial yaw rate, (c) initial low roll rate, and (d) initial high roll rate.

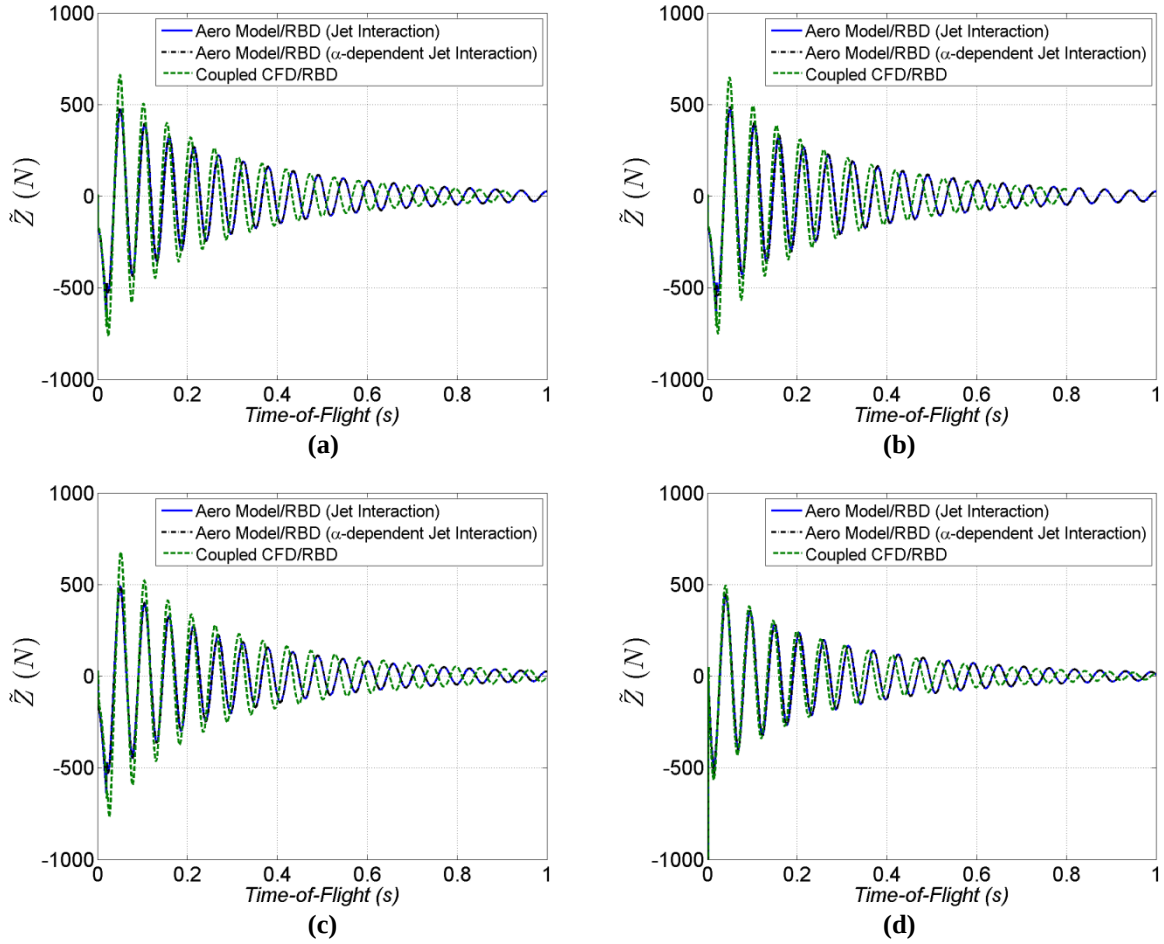

Figure 25. Time history of aerodynamic force, $\tilde{\boldsymbol{Z}}$: (a) no initial angular rate, (b) initial yaw rate, (c) initial low roll rate, and (d) initial high roll rate.

The swerving motion of the projectile center of gravity due to the jet maneuver is given in figure 26. The influence of gravity is evident in all results. The effect of the jet maneuver on the flight trajectory—in this case, the altitude—is of critical importance. Figure 26d indicates very good agreement between the altitude predictions by the aerodynamic model/RBD and the coupled method for the initial high roll rate case. For all other cases, small differences in the trajectory can be observed between the two methods. As discussed earlier, especially for the initial yaw rate and low initial roll rate cases, properly capturing how transient jet interaction effects influence the coupling between roll, pitch, and yaw is critical to highly accurate jet maneuver characterization. Differences in angular motion and axial and lateral forces between the coupled CFD/RBD and aerodynamic model/RBD methods are the main contributors to the small differences in the trajectories. Even better agreement can perhaps be achieved with an improved aerodynamic model by adding additional dependencies on aerodynamic roll angle, roll rate, pitch rate, and yaw rate, along with the traditional Mach and angle-of-attack dependencies.

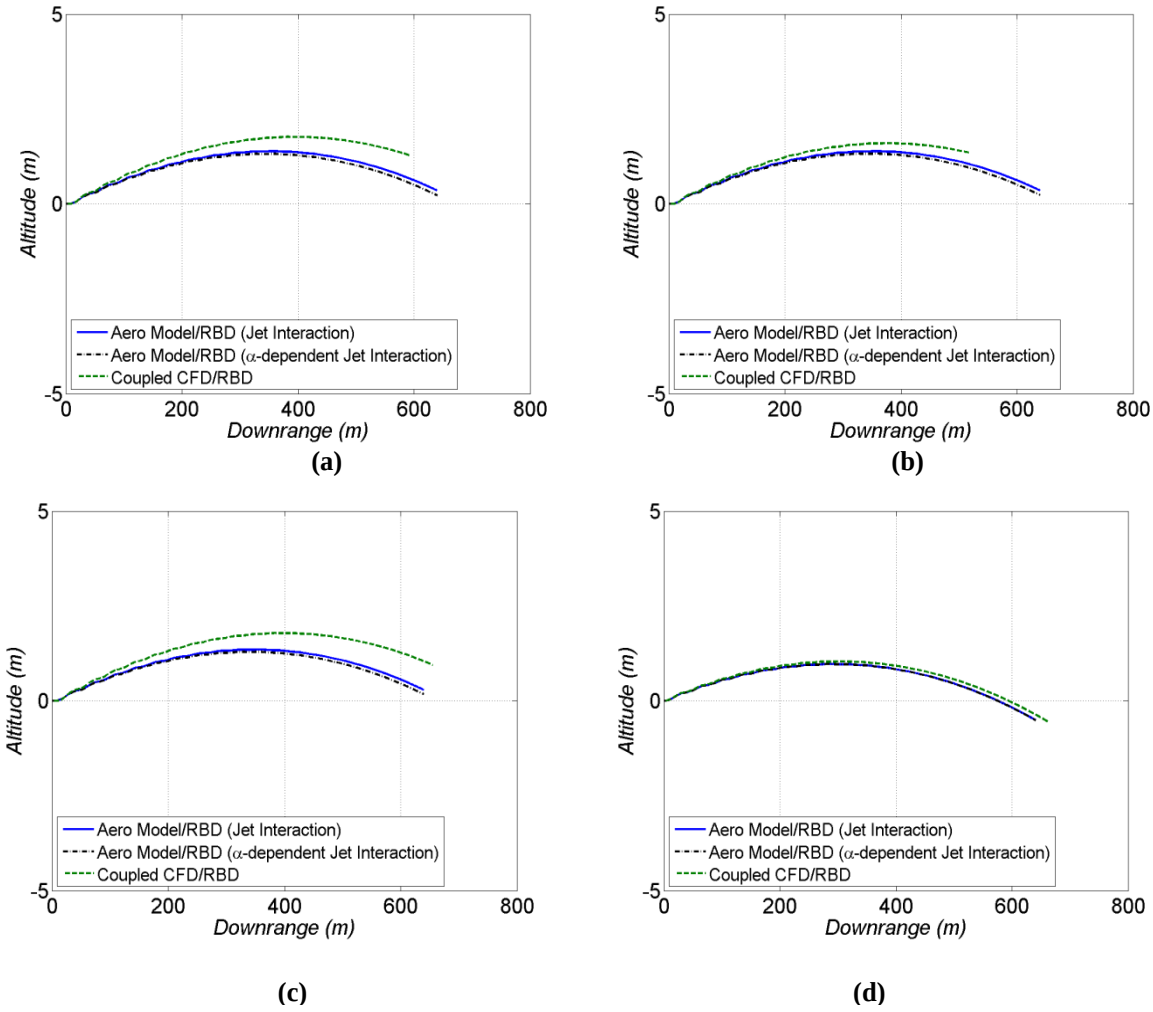

Figure 26. Altitude vs. time: (a) no initial angular rate, (b) initial yaw rate, (c) initial low roll rate, and (d) initial high roll rate.

4.4 Transient Effects During the Jet Event and Time-Accuracy of Coupled Solutions

Since spin can add to the complexities of jet interaction, one can consider the simplest case with jet interaction, i.e., the no initial angular rate case to gain further insight into the jet interaction effects. Figure 27 provides a close-up look at the transient jet effects during the jet maneuver event early in time. It corresponds to the longer duration jet that gets activated at t = 0 for 20 ms and is then turned off. Figure 27 shows the variations of the total angle of attack, the normal force in the z-direction, and the pitching moment with time. Again, the coupled results are compared with the results obtained from the aerodynamics model/RBD simulations. As seen in this figure, the aero model/RBD predictions are almost identical whether or not the angle-of-attack dependence on the jet interaction is taken into account. However, some differences can be observed between the coupled solution and the aero model/RBD result. Most of the differences seem to occur immediately after the deactivation of the jet (t > 0.02 s). The coupled results show an increase in the angle of attack by a couple of degrees resulting from larger changes in the

Z force and the pitching moment peaking at t = 0.025 s. The disagreement may be largely attributable to differences in the angle-of-attack dependency of the aerodynamics between the two methods. These effects become smaller with increase in time. Transient effects seem to be small since there is good agreement between the coupled results and the aero model/RBD results during the transient jet activation and the duration when the jet is on (t < 0.02 s). The effect of ramping in the aero model/RBD results was investigated and did not appreciably affect the results.

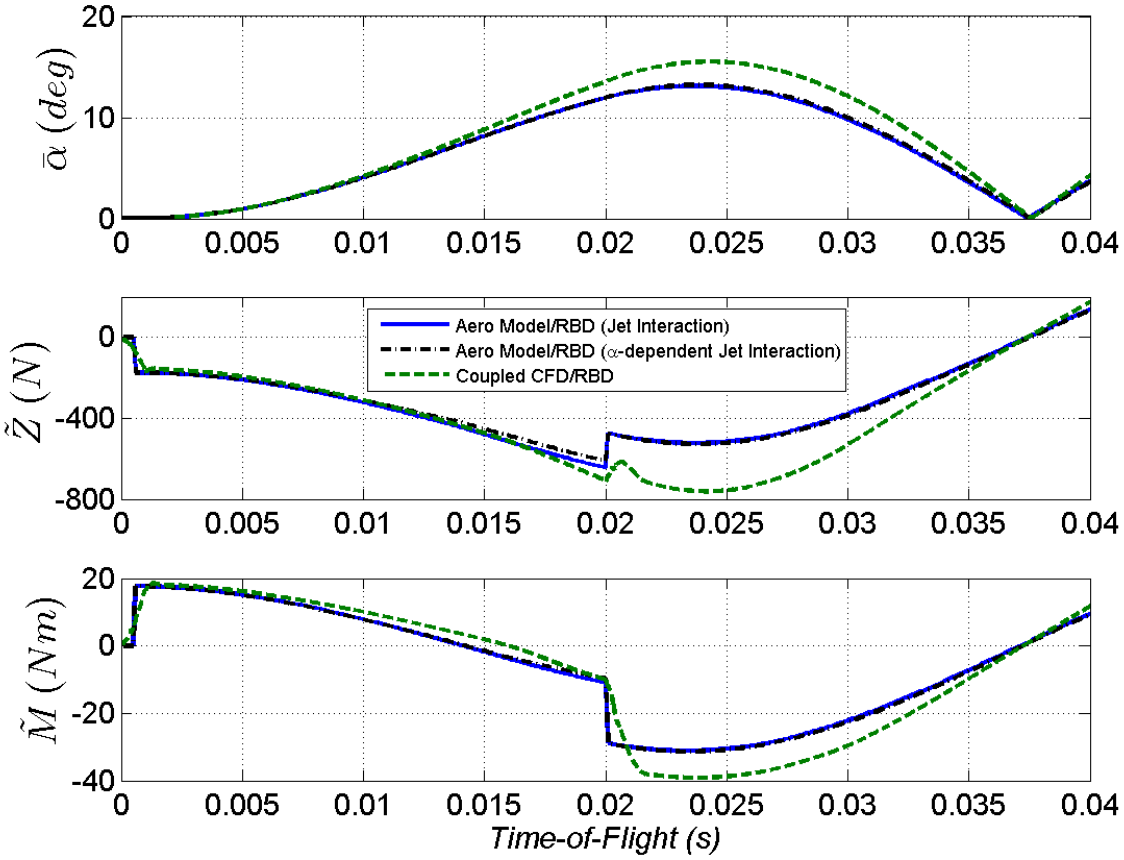

Figure 27. Transient effects of jet maneuver event for the no initial angular rate case.

As discussed earlier, small time steps were used for the coupled computations with the transient jet maneuvers. Some attempts have been made to determine if the coupled results possess the desired time accuracy. The most difficult case in this regard is the initial low roll rate case. Time step in this case was reduced by more than a factor of three from 6.9444e-05 to 2.0e05 s, and this case was rerun. Coupled results obtained from these cases are compared and shown in figure 28. These comparisons include the roll rate, roll angle, aerodynamic force in the normal direction (containing the jet), and the attitude. The differences are minor in the roll angle and the roll rate and the predicted results are almost identical for the normal force and the attitude. These comparisons clearly indicate that the time steps chosen are small enough and are sufficient to address the transients associated with the interaction between the jet and the projectile dynamics.

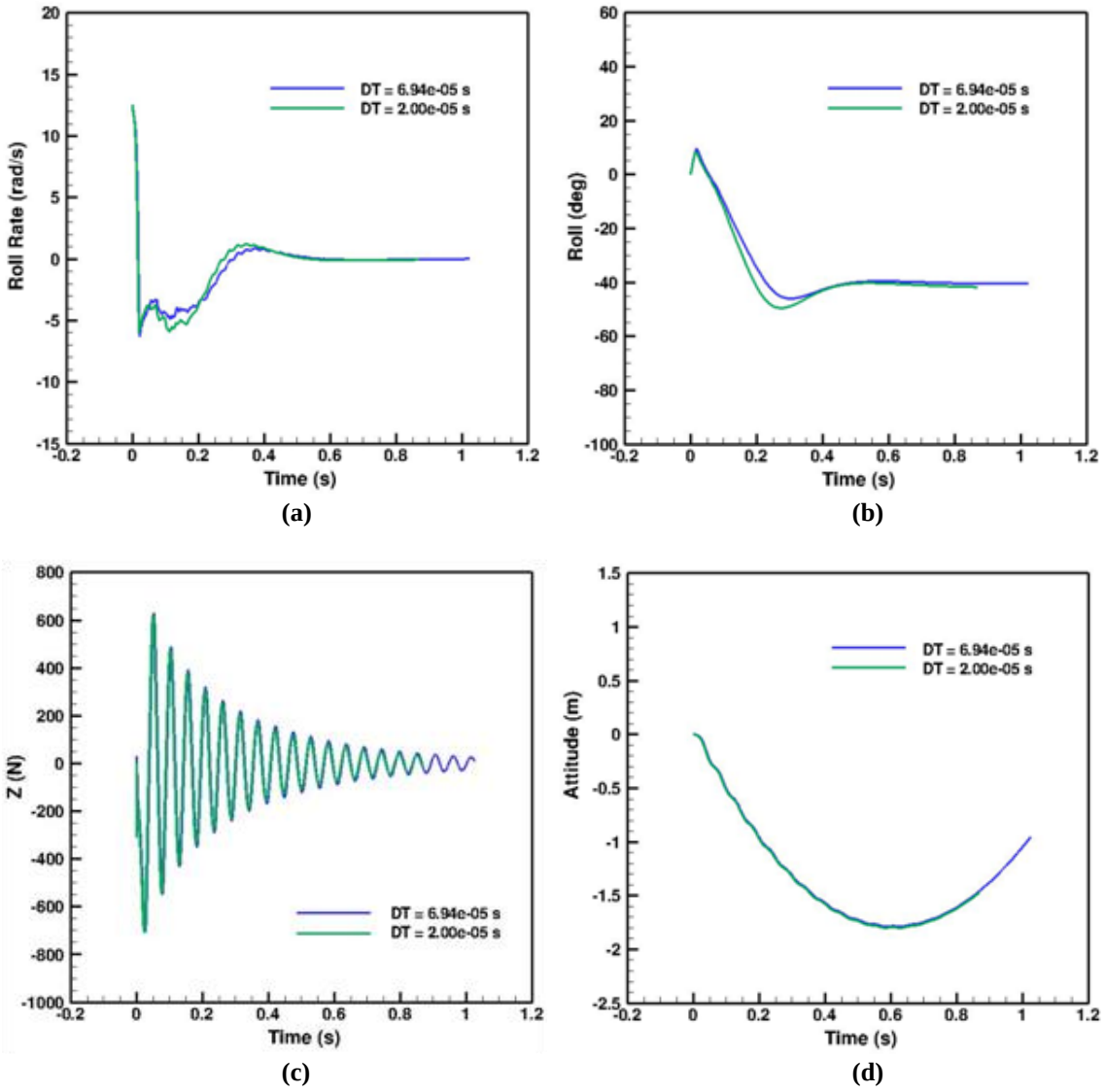

Figure 28. Effect of time step on the coupled solution for the initial low roll rate case: (a) roll rate, (b) roll angle, (c) aerodynamic force in z-direction, and (d) attitude.

5. Conclusions

Advanced virtual fly-out simulations have been performed to simultaneously compute the unsteady free-flight aerodynamics and flight dynamics of a finned projectile with jet control. Numerical solutions have been obtained using a coupled CFD/RBD procedure and a 3-D, unsteady, unstructured, Navier-Stokes computational technique with a new time-dependent jet boundary condition. A pulse jet was used and activated only once in the beginning of the flight.

Coupled CFD/RBD simulations reveal complex flow fields and projectile flight behaviors. Asymmetries due to the projectile rolling, pitching, or yawing through the jet at angle of attack affect the flight dynamics of the projectile. Roll response, and thereby jet thrust vectoring, are dictated by these flow asymmetries. Jet interaction effects alter the lateral forces and moments and ultimately the angular motion and projectile center-of-gravity swerving. Fundamentally understanding these phenomena is essential to enhancing the accuracy and efficiency (e.g., reducing number of thrusters required) of guided projectile flight.

Coupled CFD/RBD results for various cases show the time-dependent response of the finned projectile and are compared with the response obtained from aerodynamic model/RBD simulations. Jet maneuvers generally show reasonable agreement between the two different methods. However, some basic phenomena may still be missing from the current aerodynamic model/RBD method. Even better agreement can perhaps be achieved with an improved aerodynamic model by adding additional dependencies on aerodynamic roll angle, roll rate, pitch rate, and yaw rate, along with the traditional Mach and angle-of-attack dependencies. An attempt was made to include the jet interaction effects due to angle of attack in the aerodynamic model/RDB method; however, angle-of-attack effect was found to be almost negligible. There are differences in the basic aerodynamics between the methods even for the flights without the jet. Small differences observed in the predicted results by the two methods are likely due to the differences in the aerodynamics between the methods. Future study will incorporate an improved aerodynamic model/RBD and use the same basic aerodynamics to obtain better comparison of the two methods.

As for the coupled CFD/RBD procedure, a capability has been developed for virtual fly-out simulation of flights with a jet maneuver. Further work is needed to extend its capability to transonic/subsonic speed regimes. Further research is also needed to allow multiple jet activation and deactivation during the flight. With the addition of a FCS capability, this technique can also be extended for virtual fly-out simulations of guided trajectory control with pulse jets in the near future. Multiple nozzles could be used in future numerical studies, and, as needed, each nozzle jet can be turned on and off in the coupled CFD/RBD/FCS simulation for guided jet control flights.

6. References

1. Sahu, J. *Unsteady Numerical Simulations of Subsonic Flow Over a Projectile With Jet Interaction;* American Institute of Aeronautics and Astronautics (AIAA) Paper 2003-1352. Presented at AIAA Aerospace Sciences Meeting, Reno, NV, 6–9 January 2003.
2. Silton, S. Navier-Stokes Computations for a Spinning Projectile from Subsonic to Supersonic Speeds. *AIAA Journal of Spacecraft and Rockets* **2005,** *42* (2), 223–231.
3. Sahu, J. Time-Accurate Numerical Prediction of Free-Flight Aerodynamics of a Finned Projectile. *AIAA Journal of Spacecraft and Rockets* **2008,** *45* (5), 946–954.
4. Sahu, J.; Heavey, K. R. Time-Accurate Computations for Rapid Generation of Missile Aerodynamics. Presented at AIAA Atmospheric Flight Mechanics Conference, Toronto, Canada, 2–6 August 2010.
5. Weinacht, P. *Coupled CFD/GN&C Modeling for a Smart Material Canard Actuator;* AIAA Paper 2004-4712. Presented at AIAA Atmospheric Flight Mechanics Conference, Providence, RI, 2004.
6. Massey, K. C.; Guthrie, K. B. *Optimized Guidance of a Supersonic Projectile Using Pin Based Actuators;* AIAA Paper 2005-4966. Presented at AIAA Applied Aerodynamics Conference, Toronto, Canada. 2005.
7. Dykes, J.; Montalvo, C.; Costello M.; Sahu J. Use of Microspoilers for Control of Finned Projectiles. *Journal of Spacecraft and Rockets* **2012,** *49* (6), 1131–1140.
8. Smith, B. L.; Glezer, A. The Formation and Evolution of Synthetic Jets. *Journal of Physics of Fluids* **1998,** *10* (9), 2281–2297.
9. Sahu, J.; Heavey, K. R. Unsteady CFD Modeling of Micro-Adaptive Flow Control for an Axisymmetric Body. *International Journal of Computational Fluid Dynamics* **2006,** *20* (5), 271–278.
10. Fresconi, F. E. Guidance and Control of a Projectile With Reduced Sensor and Actuator Requirements. *Journal of Guidance, Control, and Dynamics* **2011,** *34* (6), 1757–1766.
11. Fresconi, F. E.; Harkins, T. Experimental Flight Characterization of Asymmetric and Maneuvering Projectiles From Elevated Gun Firings. *Journal of Spacecraft and Rockets* **2012,** *49* (6), 1120–1130.
12. Cooper, G. R.; Fresconi, F. E.; Costello, M. Flight Stability of an Asymmetric Projectile With Activating Canards. *Journal of Spacecraft and Rockets* **2012,** *49* (1), 130–135.

13. Fresconi, F. E.; Cooper, G. R.; Celmins, I.; DeSpirito, J.; Costello, M. Flight Mechanics of a Novel Guided Spin-Stabilized Projectile Concept. *Journal of Aerospace Engineering* **2012,** *226* (3), 327–340.

14. Sahu, J. *Time-Accurate Computations of Free-Flight Aerodynamics of a Spinning Projectile With and Without Flow Control;* ARL-TR-3919; U.S. Army Research Laboratory: Aberdeen Proving Ground, MD, September 2006.

15. Sahu, J. Unsteady Free Flight Aerodynamics of a Spinning Projectile at a High Transonic Speed. Presented at AIAA Atmospheric Flight Mechanics Conference, Honolulu, HI, 18–22 August 2008.

16. Sahu, J. Computations of Unsteady Aerodynamics of a Spinning Body at Transonic Speeds. Presented at 27th AIAA Applied Aerodynamics Conference, San Antonio, TX, 22–25 June 2009.

17. Sahu, J. Virtual Fly-Out Simulations of a Spinning Projectile from Subsonic to Supersonic Speeds. Presented at AIAA Applied Aerodynamics Meeting, Honolulu, HI, June 2011.

18. Sahu, J. Unsteady Aerodynamic Simulations of a Canard-Controlled Projectile at Low Transonic Speeds. Presented at AIAA Atmospheric Flight Mechanics Conference, Portland, OR, August 2011.

19. Pulliam, T. H.; Steger, J. L. On Implicit Finite-Difference Simulations of Three-Dimensional Flow. *AIAA Journal* **1982,** *18* (2), 159–167.

20. Sahu, J.; Costello, M.; Montalvo, C. *Development and Application of Multidisciplinary Computational Techniques for Projectile Aerodynamics;* Paper No. ICCFD7-4504. Presented at the 7th International Conference on Computational Fluid Dynamics, Big Island, HI, July 2012.

21. Ericsson, L. E.; Reding, J. P. Steady and Unsteady Vortex-Induced Asymmetric Loads on Slender Bodies. *Journal of Spacecraft and Rockets* **1981,** *18* (2), 97–109.

22. Brandeis, J.; Gill, J. Experimental Investigation of Side-Jet Steering for Supersonic and Hypersonic Missiles. *Journal of Spacecraft and Rockets* **1996,** *33* (3), 346–352.

23. Brandeis, J.; Gill, J. Experimental Investigation of Super- and Hypersonic Jet Interaction on Missile Configurations. *Journal of Spacecraft and Rockets* **1998,** *35* (3), 296–302.

24. Graham, M. J.; Weinacht, P. Numerical Investigation of Supersonic Jet Interaction for Axisymmetric Bodies. *Journal of Spacecraft and Rockets* **2000,** *37* (5), 675–683.

25. Graham, M. J.; Weinacht, P.; Brandeis, J. Numerical Investigation of Supersonic Jet Interaction for Finned Bodies. *Journal of Spacecraft and Rockets* **2002,** *39* (3) 376–383.

26. DeSpirito, J. Lateral Jet Interaction on a Finned Projectile in Supersonic Flow. Presented at the AIAA 50th Aerospace Sciences Conference, Nashville, TN, January 2012.

27. DeSpirito, J. *Transient Lateral Jet Interaction Effects on a Generic Fin-Stabilized Projectile;* AIAA Paper No. 2012-2907. Presented at the 30th AIAA Applied Aerodynamics Conference, New Orleans, LA, June 2012.

28. Peroomian, O.; Chakravarthy, S.; Goldberg, U. *A Grid-Transparent Methodology for CFD;* AIAA Paper 97-07245. Presented at the AIAA Aerospace Sciences Meeting, Reno, NV, 1997.

29. Peroomian, O.; Chakravarthy, S.; Palaniswamy, S.; Goldberg, U. *Convergence Acceleration for Unified-Grid Formulation Using Preconditioned Implicit Relaxation;* AIAA Paper 98-0116. Presented at the AIAA Aerospace Sciences Meeting, Reno, NV, 1998.

30. Goldberg, U. C.; Peroomian, O.; Chakravarthy, S. A Wall-Distance-Free k-ε Model With Enhanced Near-Wall Treatment. *ASME Journal of Fluids Engineering* **1998,** *120,* 457–462.

31. Batten, P.; Goldberg, U.; Chakravarthy, S. *Sub-Grid Turbulence Modeling for Unsteady Flow With Acoustic Resonance;* AIAA Paper 00-0473. Presented at 38th AIAA Aerospace Sciences Conference, Reno, NV, January 2000.

32. Murphy, C. H. *Free Flight Motion of Symmetric Missiles;* BRL Report No. 1216; U.S. Army Ballistics Research Laboratory: Aberdeen Proving Ground, MD, July 1963.

33. Bhagwandin, V.; Sahu, J. *Numerical Prediction of Pitch Damping Derivatives for a Finned Projectile at Angles of Attack;* AIAA-2012-691. Presented at the 50th AIAA Aerospace Sciences Conference, Nashville, TN, January 2012.

34. Dupuis, A. Hathaway, W. *Aeroballistic Range Tests of the Basic Finner Reference Projectile at Supersonic Velocities;* DREV-TM-9703; Defense Research Establishment: Valcartier, Canada, August 1997.

35. *GRIDGEN User Manual;* Pointwise, Inc.: Fort Worth, TX, 2009.

List of Symbols, Abbreviations, and Acronyms

D =	diameter
S =	reference area
m =	mass
$\vec{I}$	moment of inertia tensor
$\vec{I}$	moment of inertia tensor
$V, \vec{V}_{CG/I}$	total velocity of projectile; velocity of center of gravity with respect to inertial frame
Q	dynamic pressure
M	Mach number
$\alpha, \beta, \bar{\alpha}$	pitch, yaw, total angle of attack
X, Y, Z	aerodynamic and/or jet forces acting on projectile
X_G, Y_G, Z_G	gravity forces acting on projectile
L, M, N	aerodynamic and/or jet moments acting on projectile
C_X	axial force coefficient
C_N	normal force coefficient
C_{l_p}	roll damping moment coefficient
C_m	pitching moment coefficient
C_{m_q}	pitch damping moment coefficient
C_{Y_p}	dynamic side force coefficient
C_{n_p}	dynamic side moment coefficient
ϕ_A	aerodynamic roll angle
x, y, z	inertial position
$\dot{x}, \dot{y}, \dot{z}$	inertial translational velocity
u, v, w	body-fixed coordinate system translational velocity

$\dot{u}, \dot{v}, \dot{w}$	time rate of change of body-fixed coordinate system translational velocity
$\tilde{u}, \tilde{v}, \tilde{w}$	fixed-plane coordinate system translational velocity
ϕ, θ, ψ	Euler angles
$\dot{\phi}, \dot{\theta}, \dot{\psi}$	time rate of change of Euler angles
p, q, r	body-fixed coordinate system rotational velocity
$\dot{p}, \dot{q}, \dot{r}$	time rate of change of body-fixed coordinate system rotational velocity
q_0, q_1, q_2, q_3	quaternions
$\dot{q}_0, \dot{q}_1, \dot{q}_2, \dot{q}_3$	time rate of change of quaternions
x_B, y_B, z_B	body-fixed coordinate system
$\vec{V}_{CG/I}$	velocity of center of gravity with respect to inertial frame

1 (PDF) DEFENSE TECHNICAL INFORMATION CTR DTIC OCA

2 (PDF) DIRECTOR US ARMY RESEARCH LAB RDRL CIO LL IMAL HRA MAIL & RECORDS MGMT

1 (PDF) GOVT PRINTG OFC A MALHOTRA

1 (PDF) DIR USARL RDRL WML E J SAHU